



***Ab initio* spatial coupled-mode theory of Fano resonances in optical responses of multilayer interference resonators**


Dmitry V. Nesterenko ^{1,2,*}, Shinji Hayashi ^{3,4} and Victor Soifer^{1,2}

¹*Diffraction Optics Laboratory, Image Processing Systems Institute – Branch of the Federal Scientific Research Centre “Crystallography and Photonics” of Russian Academy of Sciences, Samara 443001, Russia*

²*Institute of Informatics and Cybernetics, Samara National Research University, Samara 443086, Russia*

³*Department of Electrical and Electronic Engineering, Graduate School of Engineering, Kobe University, Kobe 657-8501, Japan*

⁴*Optics and Photonics Center, Moroccan Foundation for Science, Innovation and Research (MAScIR), University Mohammed VI Polytechnic, Rabat 10100, Morocco*

 (Received 12 November 2021; revised 13 March 2022; accepted 13 July 2022; published 10 August 2022)

To reveal origins of resonance characteristics of multilayer interference structures, we developed an *ab initio* spatial coupled-mode theory using the approximations of general electromagnetic theory of wave propagation in stratified media. In contrast to the conventional coupled-mode theory, the coefficients of developed coupled-mode models, which describe the Fano resonance behavior of interference field enhancement, are given by analytical functions of structural and optical parameters of the resonance systems. The results of analytical modeling of low- and high-loss resonator systems supporting waveguide, Fabry-Pérot, symmetric, and antisymmetric plasmonic normal modes agree very well with electromagnetic numerical simulations. We demonstrate also that the conventional spatial phenomenological coupled-mode theory is accurate only for low-loss structures.

DOI: [10.1103/PhysRevA.106.023507](https://doi.org/10.1103/PhysRevA.106.023507)

I. INTRODUCTION

Optical resonances attract significant attention in the fields of sensing, optical filtering, spectroscopy, and laser optics. Photonic resonators are widely used as basic elements in many practical photonic devices [1–4]. The electromagnetic (EM) modes supported by single units can couple each other when the units are in close proximity. The coupled systems support hybrid modes with behavior different from that of the uncoupled modes. The various forms of resonance responses can be generated by controlling the coupling strength [5,6]. Understanding the nature of the resonances generated in the near and far fields of single and coupled optical resonance systems is of fundamental importance.

The resonance effects in interference or diffractive systems can be numerically simulated by a variety of solvers within the rigorous EM theory. Analytical solutions can be easily obtained in frequency domain for one-dimensional planar structures by using 2×2 transfer matrix methods [7,8]. Simulations of complex two- and three-dimensional structures in the vast majority of cases require implementation of different time- and resource-consuming numerical methods based on the rigorous EM theory, e.g., rigorous coupled-wave analysis RCWA [9], finite difference methods [10], and finite element methods [11,12]. These approaches allow us to obtain spatial distributions of amplitudes of local fields or plane waves, but they require repeating computations over a discrete set of spectral parameters to obtain key spectral information. Since analyses of coupled resonance structures within these

approaches provide overall results, it is difficult to extract directly the individual effects associated with the excitation and coupling of modes in the structures. Therefore, the approaches are not suited for gaining insights into the nature of resonance processes and formation of resonance line shapes [4,13–17]. Besides that, the traditional numerical approaches based on repeating computations demonstrate a low efficiency in complex and nonlinear optical problems.

Among various resonance effects in resonance structures, Fano resonances exhibiting asymmetric line shapes have attracted much interest in recent years. Originally the Fano resonance was explained in terms of a quantum interference between a continuum and a discrete state [13,14]. To reveal the origins of the Fano resonance in optical resonance structures, coupled-mode theory (CMT) [4,18–20] was developed by introducing the notions of EM modes supported by the elements of complex structures and describing their coupling mechanisms in the form of first-order differential equations. Coupled-mode (CM) models can describe the fields exhibiting both resonance and nonresonance behaviors of the amplitudes. The development of fast and resource-effective CMT-based formalisms is especially important in three-dimensional linear and nonlinear applications [4,21], e.g., design and optimization of integrated photonic components for optical computing, trapping, switching, enhanced spectroscopies, etc. Conventional temporal CMT [18,21–28] approaches were initially developed in the waveguide optics for analyzing the power transfer between modes, as well as power incoupling and outcoupling processes. A conventional spatial CMT framework [29] was presented to describe reflection, transmission, scattering, and absorption in the interference and diffraction optics. The coupling

*nesterenko@ssau.ru

mechanisms between the fields in coupled optical systems can be also qualitatively explained by the classical model of coupled harmonic oscillators (COs) in the form of second-order equations [30–32]. In our previous studies, we have demonstrated that the Fano resonances in angular attenuated total reflection (ATR) spectra of multilayer planar coupled plasmonic-waveguide and waveguide-waveguide systems can be well described by the CO model [33,34]. The coupling coefficients in the CM and CO models are introduced independently from the parameters of structures as constants to be estimated *a posteriori* by fitting procedures [19,20,35–37]. Therefore, the phenomenological approaches based on the CM and CO models do not allow one to obtain relationships between the parameters of structures and characteristics of their resonance effects. Moreover, these simplified representations can be efficient in high-quality-factor (Q) resonances, while they are violated in low- Q coupled resonances, which are strongly influenced by nonresonance contributions and high losses. To overcome these limitations, several *ab initio* methods, based on implementing Maxwell's equations, the Feshbach technique [38], and quasinormal modes (QNM) expansion, were proposed in time domain to develop rigorous temporal CMT [4,39] and temporal quasinormal coupled mode theory (QCMT) formalisms [40,41]. In contrast to these theories in time domain, those in the spatial domain are not yet well developed. To perform rigorous design and analysis of resonance coupled systems in spatial domain, it is highly demanded to develop a spatial CMT from first principles to provide an analytical description of coupling formalism.

Recently, we proposed an alternative approach for constructing a spatial CMT for planar two- and three-layer structures supporting surface plasmon polaritons (SPPs) at metal-dielectric interfaces [15,42], and for three- and five-layer metal-insulator-insulator (MIM) structures supporting Fabry-Pérot modes [43]. We obtained Fano approximations for resonances in angular spectra by using Taylor series of Fresnel coefficients. Based on these approximations, we constructed CM models and determined the coefficients of CM equations for the resonance and nonresonance field components expressed by analytical functions of geometrical and optical parameters of the structure. Using the developed spatial CM models we explored various resonance effects in the multilayer systems. Namely, we demonstrated shifts of SPP propagation constant from the intrinsic values caused by the absorption and SPP self-coupling through the adjacent layers, and a reversal of shift direction depending on the stacking order of the layers [15]. Furthermore, we clarified the influence of losses in structures on the shift of propagation constant of Fabry-Pérot modes [43]. Although the general form of the obtained CM models appears to be the same, the derived analytical expressions for coupling coefficients differ from case to case. In addition to the SPP and Fabry-Pérot modes discussed in our previous papers [15,43], there exists a variety of EM normal modes supported by three-layer structures, i.e., waveguide (WG) modes excited by evanescent waves [44], Fabry-Pérot modes excited by propagating waves [45], symmetric and antisymmetric plasmonic modes generated in metal-dielectric-metal or dielectric-metal-dielectric structures originating from coupling of two SPPs and excited by p -polarized light [46,47]. Even though the excitation of these

EM modes in multilayer interference systems by plane waves were widely described in the literature, no systematic analysis based on the spatial CMT was reported so far to describe resonance and coupling effects related with the modes. Extensions of our previous spatial CM models to more general cases are highly required.

In this work, we develop a generalized and analytically validated spatial CMT based on rigorous EM theory for multilayer interference resonance systems. We provide formal definitions in Sec. II A and derive analytical approximations for resonance and nonresonance components in the field amplitudes from rigorous EM expressions in Sec. II B. Fano expressions for amplitudes of internal and external fields in three-layer and four-layer resonator systems are obtained in Sec. II B and Sec. II C, respectively. Based on these approximate expressions we derive the principal equations of the spatial CMT in Sec. III A and Sec. III B, respectively. In Sec. IV we validate the spatial CM models by comparing the CM-based predictions with rigorous EM simulations for three-, four-, and six-layer interference structures supporting different kinds of the interference modes and demonstrate the accuracy of our spatial CMT for various loss levels. The CM simulations with constant coupling coefficients demonstrate the inherent inaccuracy of conventional CMT. In contrast to the conventional CMT, our CM models treat all nonresonance components generated in optical interference systems that eliminate an assumption on weakly coupled high- Q resonances. The present framework of analytical CM analysis developed for coupled interference resonators brings strong consistency to CMT, provides powerful tools for analyzing the resonance origins, and leads to physical insights into resonance effects.

II. APPROXIMATIONS WITHIN ELECTROMAGNETIC THEORY

In this section, extending our analytical approach for development of spatial CM models for multilayer structures and using the 2×2 transfer matrix method, we obtain generalized approximations for the resonance field enhancement associated with the excitation of the normal modes supported by a central layer (core) with a finite thickness sandwiched between two semi-infinite layers (clads). The mode field of this three-layer structure is established as a result of the interference of two plane waves propagating in forward and backward directions in the middle layer and is accompanied by outgoing plane waves in the clad layers. The modes of this type will be further referred to as interference modes, and the multilayer structures incorporating the systems, which support the interference modes, will be further referred to as multilayer interference resonators. To model the excitation in ATR configurations, we also consider a four-layer geometry.

A. Interference modes of three-layer systems

In this subsection, we briefly outline the type of interference modes, which can be supported by three-layer structures. Consider a general case of field excitation in three-layer structures as schematically shown in Fig. 1. In the multilayer system, the layer L_l sandwiched between two semi-infinite

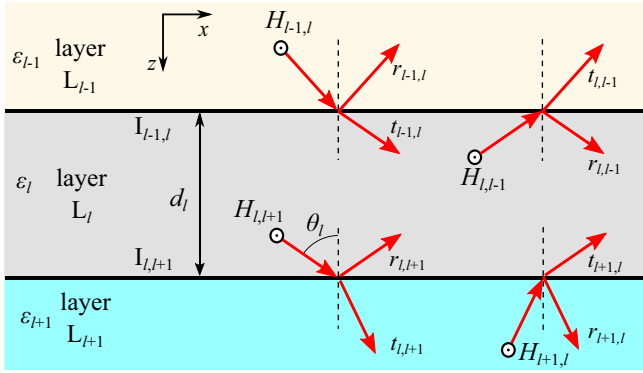


FIG. 1. Refraction and reflection of plane waves at the interfaces in a planar multilayer stack. Each layer L_k is characterized by the dielectric constant ϵ_k . The complex amplitude of the harmonic wave in k th layer L_k incident on the interface $I_{k,k+1}$ is denoted as $H_{k,k+1}$ with the reflection $r_{k,k+1}$ and transmission $t_{k,k+1}$ coefficients and that in the layer L_{k+1} incident on the interface $I_{k+1,k}$ as $H_{k+1,k}$ with the reflection $r_{k+1,k}$ and transmission $t_{k+1,k}$ coefficients.

layers L_{l-1} and L_{l+1} has a thickness of d_l . H denotes the amplitude of magnetic or electric fields in the cases of p or s polarizations, respectively.

The exciting wave $h_{l-1}^+(x, z, \alpha) = H_{l-1,l} \exp[ik_0(\alpha x + \beta_{l-1}(\alpha)z)]$ translating the field excitations in positive direction along the axis z in the layer L_{l-1} with the amplitude $H_{l-1,l}$ generates an interference field h_l inside the layer L_l due to multiple reflections of the transmitted field between the interfaces $I_{l-1,l}$ and $I_{l,l+1}$ that can be written as (details can be seen in Appendix A)

$$h_l(x, z, \alpha) = H_{l,l+1}(\alpha) \exp(ik_0\alpha x) [r_{l,l+1} - 1] \times \left[\frac{\exp[-ik_0\beta_l(z - d_l)]}{\exp[ik_0\beta_l(z - d_l)]} \right], \quad (1)$$

where the x and z components of the propagation constant are given by $k_0\alpha$ and $k_0\beta_l$, respectively; $k_0 = 2\pi/\lambda_0$ is the wave number of free space, λ_0 is the wavelength in free space; α and $\beta_l = \sqrt{\epsilon_l - \alpha^2}$ will be referred to as normalized propagation constants along the x and z axes, respectively. For $\alpha^2 > \text{Re}(\epsilon_l)$, β_l has a nonzero imaginary part, which leads to the exponential decay of the wave amplitude away from the interface along the z axis. Such plane waves are referred to as evanescent.

As we are interested in the extraction of resonance and nonresonance patterns of amplitude from the field behavior, we will focus on obtaining the approximations of the total field amplitude $H_{l,l+1}(\alpha)$. The exact solutions for the exited field in layered structures are obtained for a particular α by using 2×2 transfer matrix approach [7]. The analytic derivations summarized in Appendix A suggest that the interference field amplitude enhancement (FAE) can be represented as

$$h_l/h_{l-1}^+ = H_{l,l+1}(\alpha)/H_{l-1,l} = \chi_l \nu_l t_{l-1,l}, \quad (2)$$

where $\nu_l = \exp(ik_0\beta_l d_l)$ is the transfer coefficient that describes the correlation between the field amplitudes at the interfaces $I_{l-1,l}$ and $I_{l,l+1}$ in the layer L_l . A field generation coefficient χ_l is represented as $\chi_l(\alpha) = \sigma_l^{-1}(\alpha)$, where a

phase-matching coefficient σ_l for the waves reflecting within the middle layer is given by

$$\sigma_l(\alpha) = 1 - \nu_l^2 r_{l,l-1} r_{l,l+1}. \quad (3)$$

The expression of σ_l allows us to predict the existence of EM modes supported by the three-layer structure. For $\sigma_l \rightarrow 0$, $\chi_l \rightarrow \infty$, and the field amplitude h_l in the middle layer exhibits a resonance behavior according to Eq. (2). Suppose that $\sigma_l \rightarrow 0$ holds for $\alpha \rightarrow \gamma$. The mode excitation condition

$$\sigma_l(\gamma) = 0 \quad (4)$$

is fulfilled at a certain value of the effective refractive index of the mode $\gamma = \gamma' + i\gamma''$.

In the case $0 < \gamma'^2 < \text{Re}(\epsilon_{l-1}), \text{Re}(\epsilon_l), \text{Re}(\epsilon_{l+1})$, the dispersion relation (4) describes the excitation of radiative Fabry-Pérot modes [45]. For $\text{Re}(\epsilon_{l-1}), \text{Re}(\epsilon_{l+1}) < \gamma'^2 < \text{Re}(\epsilon_l)$, Eq. (4) reduces to the well-known relation for the planar WG mode excitation [44,48,49]. In the cases of MIM and insulator-metal-insulator structures, it is reduced to the dispersion relations for symmetric and antisymmetric coupled SPP modes [50], as demonstrated in Appendix A. The complex effective refractive index of modes can be determined by various methods, e.g., the stable iterative procedure proposed in [51], and further, γ is considered to be known.

The spectral region $\alpha^2 > \text{Re}(\epsilon_{l-1})$ will be referred to as the evanescent region, where the complex amplitude of the evanescent wave generated in the layer L_{l-1} by the interference field in the layer L_l is defined by the reflection coefficient $r_{l-1,l}$. As the energy is not transferred in the z direction by evanescent waves, generation and translation of the field oscillations are described in optics as an evanescent-field coupling, where the coupling degree is characterized by the reflection and transmission coefficients, and transfer coefficients determine the field decay strength. In the evanescent region, $|r_{l-1,l}|^2$ may be regarded as the coefficient of near-field enhancement and can take very large values under resonance conditions. In the resonance structures, it is limited by the absorption or mode leakage in the structure as will be proven by the following analytical results. This behavior of the near-field enhancement was also discovered for SPP excitation at metal-dielectric interfaces in our previous work [15].

B. Resonant field in three-layer systems

The excitation of interference eigenmodes is associated with resonance behavior of the interference field h_l in the resonance vicinity $\alpha \rightarrow \gamma'$ as follows from the dispersion relation (4). In this subsection, to analyze the behavior of the interference and outcoupled fields in the three-layer structure we obtain approximate expressions for FAE of h_l , which is proportional to $\chi_l(\alpha)$ as defined by Eq. (2).

It is well known that the interference of a nonresonance and resonance components lead to asymmetric resonance line shapes in spectra of oscillating systems, which can be approximated by the Fano formula [13,14]. In general, a complex field amplitude $H(\alpha)$ can be represented as a sum $H(\alpha) = H^{\text{nonRes}} + H^{\text{Res}}(\alpha)$ of a nonresonance component H^{nonRes} and a resonance component $H^{\text{Res}}(\alpha) = H^{\text{nonRes}} q/(\alpha - \gamma_{\text{pole}})$, where q represents the complex amplitude of the resonance component normalized to the nonresonance component,

$\gamma_{\text{pole}} = \gamma'_{\text{pole}} + i\gamma''_{\text{pole}}$ is the pole parameter. By the zero parameter $\gamma_{\text{zero}} = \gamma'_{\text{zero}} + i\gamma''_{\text{zero}}$ and representing q as

$$q = \gamma_{\text{pole}} - \gamma_{\text{zero}}, \quad (5)$$

$H(\alpha)$ can be written as $H(\alpha) = H^{\text{nonRes}}(\alpha - \gamma_{\text{zero}})/(\alpha - \gamma_{\text{pole}})$. The intensity spectra $|H(\alpha)|^2$ can be expressed in the form of the Fano formula

$$|H(\alpha)|^2 = |H^{\text{nonRes}}|^2 [(\alpha - \gamma'_{\text{zero}})^2 + \gamma''_{\text{zero}}] / \times [(\alpha - \gamma'_{\text{pole}})^2 + \gamma''_{\text{pole}}]. \quad (6)$$

Analytical expressions for several important resonance properties can be derived using the Fano formula (6). For $\gamma''_{\text{pole}} \ll |\gamma'_{\text{zero}} - \gamma'_{\text{pole}}|$, the full-width at half-maximum (FWHM) of the Fano line shape is obtained as

$$\Gamma = 2\gamma''_{\text{pole}}. \quad (7)$$

Furthermore, the resonance dip position is located at $\alpha = \gamma'_{\text{zero}}$, maximum achievable intensity of $H(\alpha)$ is estimated as $|H(\gamma'_{\text{pole}})|^2$, and a rough estimation for the depth of resonance dip can be found as $|H^{\text{nonRes}}|^2 - |H(\gamma'_{\text{zero}})|^2$. Indeed, establishment of a direct relationship between the structural parameters and the resonance response opens prospects to the predictions and interpretation of resonances [52]. The imminent characteristics of resonances and resonance line shapes in spectra can be directly obtained from the CMT-based approximations eliminating the need in postprocessing of the spectra. The derivation of analytical expressions for these characteristics, e.g., resonance width, height, slope, and maximum field enhancement (FE), is enabled by using analytical expressions for the CM parameters [52,53]. Analytical estimations for these resonance properties are effective for fast estimation of the performance of optical structures for sensing, filtration, processing, etc. Characterization of the optical and geometrical parameters of structure can be performed using the zero and pole parameters extracted by fitting the experimentally registered data with Eq. (6).

Analysis of q can give us a basic idea on the resonance line shape of the Fano formula (6). Assuming $q = q' + iq''$, and with the aid of the normalized frequency $s = (\alpha - \gamma'_{\text{pole}})/\gamma''_{\text{pole}}$, normalized distance between the positions of pole and zero parameters $\bar{q} = q'/\gamma''_{\text{pole}}$, the damping parameter $g = (q''/\gamma''_{\text{pole}} - 1)^2$, and the intensity of nonresonance component $u = |H^{\text{nonRes}}|^2$, the expression (6) reduces to the generalized Fano function

$$|H(s)|^2 = u[(s + \bar{q})^2 + g]/(s^2 + 1). \quad (8)$$

The resonance tends to show a symmetric line shape under the following conditions. First, when the normalized amplitude of the resonance component is high as compared to the resonance damping, $|q| \gg \gamma''_{\text{pole}}$ that corresponds to $|\bar{q}| \gg 1$ or $|g| \gg 1$. Second, for the resonance components with a small real part of the normalized amplitude as compared to the mode damping γ''_{pole} , so that $q' \ll |q'' - \gamma''_{\text{pole}}| - \gamma''_{\text{pole}} \ll \gamma''_{\text{pole}}$. This case corresponds to $\bar{q} \ll g-1$ and can be interpreted as the condition on the phase of resonance response to approach $\pm\pi/2$, i.e., $|q'| \ll |q''|$. The expression (8) suggests that for $\bar{q} \rightarrow 0$ the maximum value can be estimated at $s = 0$ as $|H|_{\text{max}}^2 = u[\bar{q}^2 + g]$.

Based on this brief introduction to the advantages of Fano representation we need to implement the decomposition of $\chi_l(\alpha)$ into resonance and nonresonance components and introduce a mode excitation coefficient, which characterizes the resonance component of field. According to Eq. (3) $\chi_l(\alpha) = \sigma_l^{-1}(\alpha)$ is a function of the reflection and field transfer coefficients for waves in the layer L_l . An approximate expression of $\chi_l(\alpha)$ can be derived by applying the Taylor series decomposition to these coefficients for $\alpha \rightarrow \gamma$. In fact, from the Taylor decomposition of $r_{l,k}(\alpha)$, we obtain an approximate expression

$$\tilde{r}_{l,k}(\alpha) \underset{\alpha \rightarrow \gamma}{=} r_{l,k}(\gamma) \left[1 + \frac{2\gamma(\alpha - \gamma) + (\alpha - \gamma)^2}{\beta_k(\gamma)\beta_l(\gamma)} \bar{p}_{l,k}^2 \right], \quad (9)$$

where polarization-dependent coefficient $\bar{p}_{l,k} = 1$ in the case of s polarization and $\bar{p}_{l,k} = \gamma_{l,k}(\gamma^2 - \gamma_{l,k}^2)^{-1/2}$ in the case of p polarization, $\gamma_{l,k}$ is given by $\gamma_{l,k} = [\varepsilon_l \varepsilon_k / (\varepsilon_l + \varepsilon_k)]^{1/2}$, k stands for $l-1$ or $l+1$. The interpretation of $k_0\gamma_{l,k}$ depends on the materials of the adjacent media L_l and L_k , $k = l-1$, $l+1$. In the case of metal-dielectric interface, $k_0\gamma_{l,k}$ is the propagation constant of a SPP propagating along $I_{l,k}$. In the case of dielectric media, $k_0\gamma_{l,k}$ is the in-plane propagation constant of a plane wave, which is incident at the Brewster angle to the normal of $I_{l,k}$. On the other hand, the round-trip transfer coefficient v_l^2 is approximately expressed as

$$\tilde{v}_l^2(\alpha) \underset{\alpha \rightarrow \gamma}{=} v_l^2(\gamma) \{ 1 - 2ik_0d_l\xi_l(\alpha - \gamma)[1 + (\alpha - \gamma)/\gamma] + 2[ik_0d_l\xi_l(\alpha - \gamma)]^2 \}, \quad (10)$$

where $\xi_l = \tan\theta_l = \gamma/\beta_l(\gamma)$ and θ_l represents the angle of incidence of the forward and backward plane waves in the middle layer as shown in Fig. 1.

The field generation coefficient $\chi_l(\alpha)$ can be approximately represented as a sum $\chi_l(\alpha) \approx \chi_l^{\text{nonRes}} + \chi_l^{\text{Res}}(\alpha)$ of the nonresonance χ_l^{nonRes} and resonance $\chi_l^{\text{Res}}(\alpha)$ components. Two different solutions of χ_l^{Res} can be derived using the approximations (9)–(10). For the first solution in the vicinity of the resonance $\alpha \rightarrow \gamma'$, the resonance component $\chi_l^{\text{Res}}(\alpha)$ is associated with the excitation of the modes in both the radiative and evanescent regions for $|\gamma| \gg |\alpha - \gamma|$ and can be written as

$$\chi_l^{\text{Res}}(\alpha) = \frac{\gamma}{\alpha - \gamma} \kappa, \quad (11)$$

where

$$\kappa = -i \frac{\beta_l(\gamma)}{2\gamma^2} [k_0d_l + i\bar{p}_{l,l-1}^2\beta_{l-1}^{-1}(\gamma) + i\bar{p}_{l,l+1}^2\beta_{l+1}^{-1}(\gamma)]^{-1} \quad (12)$$

is the mode excitation coefficient. In the case of lossless media, κ is purely imaginary and determine the rate of phase change in the resonance vicinity and takes a simplified form,

$$\kappa = -i/[2(\phi_l + \phi_{l,l-1} + \phi_{l,l+1})], \quad (13)$$

where $\phi_l = k_0\gamma s$ is the phase shift for plane waves propagating a distance of $s = d_l\xi_l$ in the middle layer between the interfaces, and $\phi_{l,l-1} = \gamma(\gamma^2 - \varepsilon_{l-1})^{-1/2}\bar{p}_{j,j-1}^2\xi_l$ and

$\phi_{l,l+1} = \gamma(\gamma^2 - \varepsilon_{l+1})^{-1/2} \bar{p}_{j,j+1}^2 \xi_l$ are phase shifts caused by reflection from the interfaces $I_{l-1,l}$ and $I_{l,l+1}$, respectively. In the case of a nonzero effective refractive index $|\gamma| \gg |\alpha - \gamma|$, the approximation (11) describes rapid changes in the amplitude and phase of the mode near the resonance $\alpha \rightarrow \gamma'$.

Another approximate solution of χ_l^{Res} is obtained for $|\gamma| \ll |\alpha - \gamma|$, i.e., $\gamma/(\alpha - \gamma) \rightarrow 0$. In this case, χ_l^{Res} is described by the second-order terms of the approximations of Eqs. (9) and (10) and has the form

$$\chi_l^{\text{Res}}(\alpha) = \frac{\gamma^2}{(\alpha - \gamma)^2} \kappa. \quad (14)$$

This case corresponds to the modes with $\gamma \rightarrow 0$ that exist in the radiative region, e.g., Fabry-Pérot modes excited by propagating waves incident on the interface at angles close to the surface normal.

The background component χ_l^{nonRes} can be approximately estimated as a lower limit of the field generation coefficient $\chi_l^{\text{nonRes}} = \min_{\alpha} |\chi_l(\alpha)|$. In the evanescent region, for low-absorption materials with small values of $\text{Im}(\varepsilon_{l-1})$, $\text{Im}(\varepsilon_{l-1})$, and $\text{Im}(\varepsilon_{l+1})$, $|v_l^2 r_{l,l-1} r_{l,l+1}| \rightarrow 1.0$ that provides the maximum value of the phase matching coefficient of $\sigma_l = 2.0$ at out-of-resonance conditions. The global lower limit for a nonresonant background is found using the maximum value of σ_l as $\chi_l^{\text{nonRes}} = 0.5$.

From the above decomposition of $\chi_l(\alpha)$ into the sum of χ_l^{nonRes} and $\chi_l^{\text{Res}}(\alpha)$, the total field generated in the structure can be represented as the Fano interference $h_{l,l+1}(x, z, \alpha) = h^{\text{nonRes}}(x, z) + h^{\text{Res}}(x, z, \alpha)$ of a slowly changing continuum component h^{nonRes} and a resonance component h^{Res} . Taking into account Eq. (2), we define the resonant field h^{Res} in the middle layer L_l by a superposition of plane waves in the following form:

$$h^{\text{Res}}(x, z, \alpha) = \Psi(\alpha) \exp(ik_0 \alpha x) [r_{l,l+1} \quad 1] \\ \times \begin{bmatrix} \exp[-ik_0 \beta_l (z - d_l)] \\ \exp[ik_0 \beta_l (z - d_l)] \end{bmatrix}, \quad (15)$$

where $\Psi(\alpha)$ is the amplitude of the resonance component. $\Psi(\alpha)$ exhibits the following resonance behavior associated with the excitation of an interference mode:

$$\Psi(\alpha) = \chi_l^{\text{Res}}(\alpha) v_l t_{l-1,l} H_{l-1,l}. \quad (16)$$

At the resonance $\alpha = \gamma$, the field distribution $h^{\text{Res}}(x, z, \gamma)$ determines the core field profile of the mode. Therefore, the modes described by this formalism, the interference of the forward and backward waves, can be regarded as two-wave interference modes. In the same way, the nonresonant field h^{nonRes} can be characterized by the complex amplitude H^{nonRes} given by

$$H^{\text{nonRes}} = \chi_l^{\text{nonRes}} v_l (\gamma') t_{l-1,l} (\gamma') H_{l-1,l}. \quad (17)$$

Further, the values of reflection, transmission, and transfer coefficients are assumed to be taken at $\alpha \rightarrow \gamma'$. Let us consider here the case of a resonant mode with a nonzero propagation constant. The amplitude of the interference field $H_{l,l+1}(\alpha)$ generated in the structure can be represented as the Fano interference of the symmetric Lorentzian resonance of the complex amplitudes of the mode Ψ and

background nonresonance component H^{nonRes} as $H_{l,l+1}(\alpha) = \Psi(\alpha) + H^{\text{nonRes}}$. Using Eqs. (16) and (17) we find

$$H_{l,l+1}(\alpha) = \chi_l^{\text{nonRes}} \frac{\alpha - \gamma(1 - \kappa/\chi_l^{\text{nonRes}})}{\alpha - \gamma} v_l t_{l-1,l} H_{l-1,l}. \quad (18)$$

FE of the total field in the middle layer is given by $|H_{l,l+1}/H_{l-1,l}|^2$, and, in general, FE exhibits an asymmetric Fano line shape in spectra. For low-loss structures, the total FE spectra exhibit symmetric Lorentzian line shapes, since the imaginary part of κ is higher than the real one. Substituting $\alpha = \gamma'$ into Eq. (18), we can estimate the lower limit for the maximum FE associated with the excitation of the interference mode as

$$|\Psi(\gamma')/H_{l-1,l}|^2 = |\gamma \kappa v_l t_{l-1,l}|^2 / \gamma''^2. \quad (19)$$

The analytical expressions for the amplitudes of outcoupled fields are obtained using the transfer matrix relations summarized in Appendix A. The transmission and total reflection coefficients for the three-layer structure are found as $t_{l-1,l+1} = t_{l,l+1} H_{l,l+1}/H_{l-1,l}$ and $r_{l-1,l+1} = (r_{l-1,l} H_{l-1,l} + t_{l,l-1} H_{l,l-1})/H_{l-1,l}$, respectively. Substituting (18) into the analytical expression for the transmission coefficient results in the following approximation:

$$\tilde{t}_{l-1,l+1}(\alpha) = \chi_l^{\text{nonRes}} \frac{\alpha - \gamma(1 - \kappa/\chi_l^{\text{nonRes}})}{\alpha - \gamma} v_l t_{l-1,l} t_{l,l+1}. \quad (20)$$

Using the relation $H_{l,l-1} = v_l r_{l,l+1} H_{l,l+1}$ and Eq. (18), the approximation of the total reflection coefficient can be written as the interference of the nonresonant reflection $r_{l-1,l}$ from the $I_{l-1,l}$ interface and the Fano component of the mode response

$$\tilde{r}_{l-1,l+1}(\alpha) = r_{l-1,l+1}^{\text{nonRes}} \frac{\alpha - \gamma[1 - \kappa/r_{l-1,l+1}^{\text{nonRes}}]}{\alpha - \gamma} v_l^2 t_{l,l-1} t_{l-1,l} r_{l,l+1}, \quad (21)$$

where $r_{l-1,l+1}^{\text{nonRes}} = (r_{l-1,l} + \chi_l^{\text{nonRes}})$ is the total nonresonance component.

According to Eq. (21), the coefficients of Fano formula approximating the reflection line shape in spectra of three-layer structures supporting interference modes have similar physical origins as those derived for SPP modes at simple metal-dielectric interfaces in our previous work [15]. However, the analytical expression for the SPP excitation coefficient $\kappa_{\text{SPP}} = 2\gamma_{l,l+1}^2/(\varepsilon_l - \varepsilon_{l+1})$ (equal to κ^2 in [15]) suggests that the amplitude of SPP component depends on the permittivity values of both layers. In contrast to the SPP excitation, the excitation coefficient κ of interference modes given by Eq. (12) depends also on the resonator layer thickness.

The registration of the spectra of reflectivity $|r|^2$ and transmission $|t|^2$ of the propagation waves can be realized by far-field detectors as functions of incidence angle. In the evanescent region, direct measurements of the near-field enhancement spectra of evanescent waves are not possible. One of the approaches for detecting evanescent fields is to realize an optical structure, in which evanescent waves in a low-index media couple to propagating waves in an adjacent high-index media. Analysis of the influence of this adjacent high-index

media requires consideration of an additional layer in our model.

C. Resonant field in four-layer systems

In this section, we extend our study to the case of excitation of an interference mode in a three-layer structure separated from a semi-infinite media by a single spacer layer that does not support resonant modes. For example, this geometry can cover the excitation of guided modes supported by a waveguide in air, which is represented by a three-layer structure, using a high-index prism placed in a close proximity of the waveguide. Another example is a MIM structure in air comprising a thin metal film separated by a dielectric layer from a semi-infinite metal layer. The geometry considered here can be represented by the four-layer structure consisting of the L_{l-2} , L_{l-1} , L_l , and L_{l+1} layers, which can be regarded as a combination of the resonance three-layer structure consisting of the $L_{l-1} - L_{l+1}$ layers and a semi-infinite L_{l-2} layer; the

L_l layer is the interference layer separated from the semi-infinite L_{l-2} layer by a spacer layer L_{l-1} of the thickness d_{l-1} .

To generalize our description to a planar structure consisting of g layers, we introduce the following notation for numbering the layers. On top of the three-layer system consisting of the $L_{l-1} - L_{l+1}$ layers, we add g layers. Then, the top semi-infinite layer is assigned to the L_{l-1-g} layer and the multilayer system is excited by an incident wave in this layer. The total reflection and transmission coefficients are introduced as $r_{l-g+2,l+1} \equiv h_{l-1-g}^-/h_{l-1-g}^+$ and $t_{l-1-g,l+1} \equiv h_{l+1}^+/h_{l-1-g}^+$, where h_{l-1-g}^- and h_{l+1}^+ are the reflected and transmitted fields, respectively.

Using analytical expressions for the complex amplitude $H_{l,l+1}$ in the four-layer system, coefficients A_k , B_k , C_k , and D_k obtained by the 2×2 transfer matrix approach and resonance behavior of $D_l^{-1} = (\chi_l^{\text{Res}} + \chi_l^{\text{nonRes}})v_l t_{l-1,l}$ (details can be seen in Appendix A), we can express the amplitude of interference field as the Fano resonance

$$H_{l,l+1}(\alpha) = P \chi_l^{\text{nonRes}} v_l t_{l-1,l} b^{-1} \frac{\alpha - \gamma(1 - \kappa/\chi_l^{\text{nonRes}})}{\alpha - \gamma(1 - \kappa P)} H_{l-2,l-1}, \quad (22)$$

where $P = b/(D_{l-1} + b\chi_l^{\text{nonRes}})$ is the amplitude of the resonance modulation of the interference field, and $b = v_l t_{l-1,l} C_{l-1} B_l$ is a transfer coefficient. An approximation for the transmission coefficient of the four-layer structure is found using (22) as $\tilde{t}_{l-2,l+1}(\alpha) = t_{l,l+1} H_{l,l+1}(\alpha)/H_{l-2,l-1}$.

Substitution of the relation (22) into the expression for total reflection coefficient $r_{l-2,l+1} = (r_{l-2,l-1} H_{l-2,l-1} + t_{l-1,l-2} H_{l-1,l-2})/H_{l-2,l-1}$ leads to an approximate expression of the total reflection coefficient for the four-layer structure written as a Fano formula,

$$\tilde{r}_{l-2,l+1}(\alpha) = r_{l-2,l+1}^{\text{nonRes}} \frac{\alpha - \gamma[1 - \kappa P(r_{l-2,l-1} + t_{l-1,l-2} A_{l-1}/C_{l-1})/r_{l-2,l+1}^{\text{nonRes}}]}{\alpha - \gamma(1 - \kappa P)}, \quad (23)$$

where $r_{l-2,l+1}^{\text{nonRes}} = r_{l-2,l-1} + t_{l-1,l-2}(B_{l-1} + a\chi_l^{\text{nonRes}})P/b$ is an amplitude of the nonresonance component of the total reflection coefficient, and $a = v_l t_{l-1,l} A_{l-1} B_l$ is a transfer coefficient.

Since the relation (23) is expressed in a generalized form and it can be extended to the system of an arbitrary number of layers. In the case of four layers, Eq. (23) can be further simplified to

$$\tilde{r}_{l-2,l+1}(\alpha) = r_{l-2,l+1}^{\text{nonRes}} \frac{\alpha - \gamma[1 - \kappa P/(r_{l-2,l-1} r_{l-2,l+1}^{\text{nonRes}})]}{\alpha - \gamma(1 - \kappa P)}. \quad (24)$$

According to Eqs. (22) and (24), the reflection $|\tilde{r}_{l-2,l+1}(\alpha)|^2$ and transmission $|\tilde{t}_{l-2,l+1}(\alpha)|^2$ spectra exhibit asymmetric resonance line shapes. In the Fano formula (24), the pole and zero parameters are $\gamma_{\text{pole}} = \gamma(1 - \kappa P)$ and $\gamma_{\text{zero}} = \gamma[1 - \kappa P/(r_{l-2,l-1} r_{l-2,l+1}^{\text{nonRes}})]$, respectively. The position of a resonance dip determined by γ'_{zero} is shifted from that of the three-layer structure due to the influence of the adjacent layers.

The form of Fano expression (24) corresponds to that for SPP excitation in three-layer metal-dielectric structures in [15]. Note that the SPP Fano expression in [15] was obtained with neglecting the nonresonance component of SPP field.

III. COUPLED-MODE THEORY

A. Three-layer system

As demonstrated in the previous section, in the resonance region $\alpha \rightarrow \gamma'$, the total field generated in the three-layer

structure by an exciting plane wave $h_{l-1,l}$ with the amplitude $H_{l-1,l}$ is given by a superposition of the resonance component h^{Res} and the continuous component h^{nonRes} characterized by a nonresonance behavior of the amplitude. To describe the resonance response of the interference mode we apply the same formalism as that used for SPPs localized at metal-dielectric interfaces [15,54]. The resonant field associated with the excitation of the interference mode is considered as a product $h^{\text{Res}}(\alpha, x) = \Psi(\alpha)c(\alpha, x)\exp(ik_0\gamma x)$ of a fast $\exp(ik_0\gamma x)$ dependence and a slowly varying envelope function $c(\alpha, x)$. In the spirit of one-dimensional spatial formulation of CMT, the dynamic equation for the resonant field can be written by neglecting the first-order derivative of $c(\alpha, x)$ as $(ik_0\gamma)^{-1}(dh^{\text{Res}}/dx) = h^{\text{Res}}$. Based on expressions (16) and (17) for the mode resonance amplitude Ψ and the nonresonance amplitude H^{nonRes} the following dynamics equations for the excitation of the resonant and nonresonant

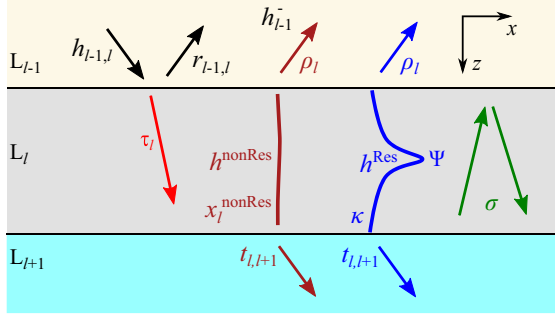


FIG. 2. Field in- and outcoupling of an interference mode in the three-layer system.

fields, h^{Res} and h^{nonRes} , in the interference resonator by the wave $h_{l-1,l}$ can be written, respectively:

$$\frac{1}{ik_0\gamma} \frac{dh^{Res}}{dx} = h^{Res} + \kappa\tau_l h_{l-1,l}, \quad (25)$$

$$h^{nonRes} = \chi_l^{nonRes} \tau_l h_{l-1,l}, \quad (26)$$

where $\tau_l = v_l t_{l-1,l}$ is an incoupling coefficient for the oscillations of the exciting wave $h_{l-1,l}$ at the interface $I_{l-1,l}$ to the resonator field at the interface $I_{l,l+1}$. Equations (25) and (26) constitute a coupled-mode model of the three-layer interference resonator. Excitation of the resonance oscillations by the exciting wave is completely described by Eq. (25). For harmonic oscillations of the exciting wave $h_{l-1,l} \propto \exp(ik_0\alpha x)$ the secondary fields are also harmonic with a propagation constant $k_0\alpha$ along the x axis. The solution of Eq. (25) leads to the representation of the complex amplitude $\Psi(\alpha)$ in the form of Eq. (16). In contrast to the conventional CMT formulations [18], the correct form of Eq. (25) suggests the frequency-dependent coefficient $(ik_0\gamma)^{-1}$ in the left-hand side.

The total field h_{l-1}^- outcoupled from the three-layer structure in the backward direction can be obtained as a superposition of a nonresonance component $r_{l-1,l} h_{l-1,l}$ originated from the reflection from the front interface $I_{l-1,l}$ and a component of the resonator field outcoupled to the layer L_{l-1} [using Eq. (A6) in Appendix A], resulting in

$$h_{l-1}^- = r_{l-1,l} h_{l-1,l} + \rho_l (h^{Res} + h^{nonRes}), \quad (27)$$

where $\rho_l = r_{l,l+1} v_l t_{l,l+1}$ is an outcoupling coefficient for the field reflected from the interface $I_{l,l+1}$ in the layer L_l into the field in the layer L_{l-1} . The graphical representation of the field coupling described by Eqs. (25)–(27) is schematically shown in Fig. 2.

According to the obtained CM model (25)–(27), the excitation of interference modes in three-layer structures can be compared to the SPP excitation at single metal-dielectric interfaces [15,42,54]. The nonresonance fields and the coupling strength between external and SPP fields were omitted in the SPP CM models. To improve the quality of physical representation the expression for nonresonance fields was included into the interference CM model. In the case of SPP composed of two evanescent waves at the metal-dielectric interface, incoming evanescent fields directly couple to a SPP, and the coupling strength between external and SPP fields

equals to one. In contrast, the coupling strength τ_l between external and interference fields in the resonator layer depends on optical and geometrical properties of the resonator layer L_l .

From the CM model (25)–(27), we can derive solutions for outcoupled fields. By substituting Eqs. (25) and (26) into the expression (27), an approximation of the total reflection coefficient $r_{l-1,l+1} = h_{l-1}^-/h_{l-1,l}$ is found to be

$$\tilde{r}_{l-1,l+1}(\alpha) = r_{l-1,l} + \chi_l^{nonRes} \frac{\alpha - \gamma(1 - \kappa/\chi_l^{nonRes})}{\alpha - \gamma} \tau_l \rho_l. \quad (28)$$

Note that the approximate expression given by Eq. (28) coincides with Eq. (21). The amplitude of the resonance component in Eq. (28) is modulated by the product of the incoupling and outcoupling coefficients $\tau_l \rho_l$.

The product $\tau_l \rho_l$ itself exhibit a resonance behavior that interfere with that of the resonance component of the reflected field and using Eq. (3) can be written as $\tau_l \rho_l = (r_{l-1,l} - r_{l-1,l}^{-1})(1 - \sigma_l)$. Analyzing σ_l we can demonstrate a resonance behavior of $\tau_l \rho_l$. With the aid of Eq. (11) the approximation of the phase matching coefficient $\sigma_l(\alpha) = \chi_l^{-1}(\alpha)$ can be written in the form

$$\tilde{\sigma}_l(\alpha) = \frac{1}{\chi_l^{nonRes}} \frac{\alpha - \gamma}{\alpha - \gamma(1 - \kappa/\chi_l^{nonRes})}. \quad (29)$$

According to the expression (29), the behavior of $\tilde{\sigma}_l$ spectrum is also described by the Fano interference. In the vicinity of the resonance $\alpha \rightarrow \gamma'$, the in-phase resonance excitation of the mode occurs at $\tilde{\sigma}_l \rightarrow 0$. The maximum value of $\tilde{\sigma}_l = (\chi_l^{nonRes})^{-1}$ is achieved, when $|\alpha - \gamma| \gg |\gamma\kappa/\chi_l^{nonRes}|$ holds, i.e., out of the resonance. Therefore, the modulation of the resonance component in Eq. (28) by in- and outcoupling $\tau_l \rho_l$ modifies the nonresonance and resonance components of $\tilde{r}_{l-1,l+1}$ in the form independent of the coupling coefficients

$$\hat{r}_{l-1,l+1}(\alpha) = \hat{r}_{l-1,l+1}^{nonRes} \frac{\alpha - \gamma(1 - \kappa(r_{l-1,l} - r_{l-1,l}^{-1})/\hat{r}_{l-1,l+1}^{nonRes})}{\alpha - \gamma}, \quad (30)$$

where $\hat{r}_{l-1,l+1}^{nonRes} = r_{l-1,l}^{-1} + (r_{l-1,l} - r_{l-1,l}^{-1})\chi_l^{nonRes}$ is the total nonresonance reflection from the three-layer structure. The approximation (30) describes asymmetric resonance line shapes in the spectral region far from the Brewster angle. The pole and zero are $\gamma_{pole} = \gamma$ and $\gamma_{zero} = \gamma\{1 - \kappa(r_{l-1,l} - r_{l-1,l}^{-1})/\hat{r}_{l-1,l+1}^{nonRes}\}$, respectively. Surprisingly, the coefficients of the Fano expression (30) do not depend on the coupling coefficients and cannot be obtained from the proposed CM model with constant coefficients. In the case of low-absorption materials $\gamma'' \ll \gamma'$, by substituting $\alpha = \gamma'_{pole}$ into the analytical expression for the reflectivity spectrum (30), we obtain an analytical expression determining an approximate maximum FE of the reflected wave given by

$$|\hat{r}_{l-1,l+1}(\alpha)|_{\max}^2 = |\hat{r}_{l-1,l+1}(\gamma'_{pole})|^2 = |\kappa(r_{l-1,l} - r_{l-1,l}^{-1})|^2 \gamma'/\gamma''^2. \quad (31)$$

In conventional CM models, the coupling coefficients are supposed to be constants. Following this common approach and fixing values of the coupling coefficients τ_l and ρ_l , we

can obtain the solution in the form (21). As we demonstrated above, the resonance behavior of $\tau_l \rho_l$ results in the modification of the resonance response from (21) to (30). In the approximate calculations of the resonance response by the present CM models, the following two approaches can be implemented. In the first case, which is further referred to as the ‘‘Fano’’ case, all the coupling coefficients are considered as constants and estimated at $\alpha = \gamma'$. In the second approach, the resonance behavior of $\tau_l \rho_l$ can be introduced by fixing τ_l and assuming the resonance behavior of $\rho_l(\alpha) = (1 - \delta_l)(1 - r_{l-1,l}^{-1})v_l^{-1}$. This case is further referred to as the ‘‘ubiquitous Fano’’ (‘‘UFano’’) case. Except that the letter ‘‘U’’ also symbolize the first initial of Fano’s name. The ‘‘Fano’’ and ‘‘UFano’’ approaches are, therefore, realized in the CM model by using the constant and variable forms of the outcoupling coefficient ρ_l , respectively, while other coefficients are fixed.

In this subsection, we succeeded in developing the CM model (25)–(27) relying on the Fano approximations for the field in three-layer structures. The CM equations and analytical expressions for the coefficients of the CM model are obtained based on simple rigorous physical principles.

B. Four-layer system

To extend the three-layer model to the four-layer case ($g = 4$), we first analyze the influence of the spacer layer L_{l-1} on the mode excitation. In Eqs. (25) and (26), $\tau_l h_{l-1,l}$ describes the mode exciting field at the interface $I_{l,l+1}$ as a result of transfer of $h_{l-1,l}$ oscillations through the layer L_l . If the mode excitation is performed through an additional layer L_{l-1} , the mode exciting field at the interface $I_{l,l+1}$ is represented as a sum of oscillations $\tau_{l-1,l} h_{l-2,l-1}$ transferred consequently through the layers L_{l-1} and L_l and the oscillations outcoupled from and incoupled back to the resonator after multiple reflections in the layer L_{l-1} . Therefore, the mode exciting field satisfies the following relation:

$$\tau_l h_{l-1,l} = \tau_{l-1,l} h_{l-2,l-1} + \eta_{l-1} (h^{\text{Res}} + h^{\text{nonRes}}), \quad (32)$$

where $\tau_{l-1,l} = \tau_{l-1} \tau_l \sigma_{l-1}^{-1}$ is a coupling coefficient of the incoming wave to the resonant and background fields, $\eta_{l-1} = \rho_l \mu_{l-1} \tau_l \sigma_{l-1}^{-1}$ is a coefficient of self-coupling of the resonator fields through the layer L_{l-1} , $\mu_{l-1} = v_{l-1}^2 r_{l-1,l-2}$ is a coefficient of back-reflection at the layer L_{l-1} , and σ_{l-1}^{-1} describes the influence of multiple reflections in the layer L_{l-1} between the interfaces $I_{l-2,l-1}$ and $I_{l-1,l}$.

The excitation of the fields h^{Res} and h^{nonRes} in the resonator layer L_l of four-layer structure by the incoming wave $h_{l-2,l-1}$ with the amplitude $H_{l-2,l-1}$ can be formulated within the framework of the coupled-mode formalism by substituting the component $\tau_l h_{l-1,l}$ determined by Eq. (32) into Eqs. (25) and (26):

$$\frac{1}{ik_0 \gamma} \frac{dh^{\text{Res}}}{dx} = h^{\text{Res}} + \kappa \tau_{l-1,l} h_{l-2,l-1} + \kappa \eta_{l-1} h^{\text{Res}} + \kappa \eta_{l-1} h^{\text{nonRes}}, \quad (33)$$

$$h^{\text{nonRes}} = \chi_l^{\text{nonRes}} \tau_{l-1,l} h_{l-2,l-1} + \chi_l^{\text{nonRes}} \eta_{l-1} h^{\text{Res}} + \chi_l^{\text{nonRes}} \eta_{l-1} h^{\text{nonRes}}. \quad (34)$$

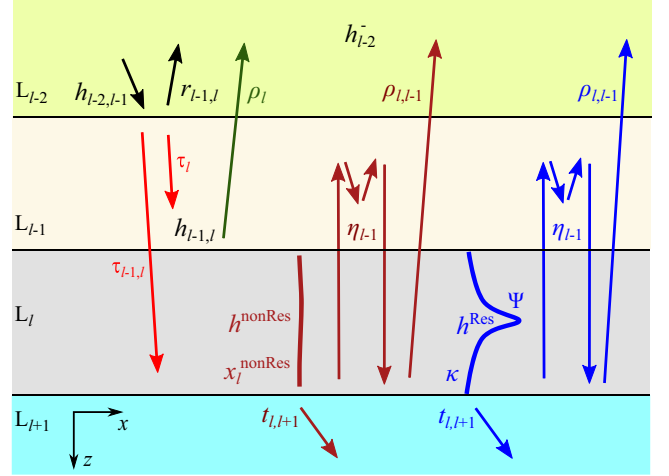


FIG. 3. In- and outcoupling of resonant and nonresonant fields in four-layer systems supporting interference modes.

Since the field associated with the mode excitation in the resonator is determined by the CM Eqs. (33) and (34), the fields in each layer and the total field h_{l-2}^- reflected from the structure can be consequently found by defining amplitude transfer coefficients using the 2×2 transfer matrix formalism (A9) described in Appendix A. We obtain the backward field h_{l-2}^- at the interface $I_{l-2,l-1}$ as

$$h_{l-2}^- = r_{l-2,l-1} h_{l-2,l-1} + \rho_{l,l-1} (h^{\text{Res}} + h^{\text{nonRes}}) + \rho_{l-1} h_{l-1,l}, \quad (35)$$

where $\rho_{l,l-1} = \rho_l v_{l-1} t_{l-1,l-2}$ is an outcoupling coefficient for the field reflected from the interface $I_{l,l+1}$ in the layer L_l into the field in the layer L_{l-2} . The impacts of field coupling coefficients introduced in Eqs. (32)–(35) are schematically shown by arrows in Fig. 3.

Consider solutions of the derived CM model (32)–(35). Substituting Eq. (34) into Eq. (33) provides a Lorentzian expression for the resonance field,

$$h^{\text{Res}}(\alpha) = \Psi_0^{(4)} \frac{\gamma \kappa}{\alpha - \gamma(1 - \kappa P)} h_{l-2,l-1}, \quad (36)$$

where $P = -\eta_{l-1}(1 - \eta_{l-1} \chi_l^{\text{nonRes}})^{-1}$ is a coefficient of the interference field back-coupling resulting from multiple reflections in the four-layer system, and $\Psi_0^{(4)} = -\tau_{l-1,l} P / \eta_{l-1} = \tau_{l-1,l} (1 - \eta_{l-1} \chi_l^{\text{nonRes}})^{-1}$ is an incoupling coefficient for an exciting wave from $I_{l-2,l-1}$ to $I_{l,l+1}$ in the four-layer case. The variation of nonresonant field originated from the multiple reflections in the adjacent layer is obtained as

$$h^{\text{nonRes}}(\alpha) = \Psi_0^{(4)} \chi_l^{\text{nonRes}} \frac{\alpha - \gamma}{\alpha - \gamma(1 - \kappa P)} h_{l-2,l-1}. \quad (37)$$

According to the expression (37), the nonresonant field h^{nonRes} is described by the Fano approximation due to the mutual interaction of the nonresonant and resonant fields supported by the back reflection in the spacer layer L_{l-1} . The Fano function (37) becomes zero at $\alpha = \gamma$ that implies minimization of the nonresonant field at the resonance. The total field

$h_{l,l+1}(\alpha) = h^{\text{Res}}(\alpha) + h^{\text{nonRes}}(\alpha)$ in the resonator is thus found as an interference of the resonant and nonresonant fields

$$h_{l,l+1}(\alpha) = \Psi_0^{(4)} \chi_l^{\text{nonRes}} \frac{\alpha - \gamma(1 - \kappa/\chi_l^{\text{nonRes}})}{\alpha - \gamma(1 - \kappa P)} h_{l-2,l-1}. \quad (38)$$

Equation (38) determines the dependence of field in the resonator on the coupling coefficients, and it is exactly the same as Eq. (22). Based on Eq. (38) an analytical expression for the maximum FE in low-loss four-layer structures $\text{FE}^{(4)}(\alpha) = |h_{l,l+1}/h_{l-2,l-1}|^2$ can be obtained assuming $\gamma' \gg \gamma''$ near the resonance $\alpha \rightarrow \gamma'$ as

$$\text{FE}^{(4)}(\gamma') = |\tau|^2 |\eta_{l-1} - \gamma''(i\gamma\kappa + \chi_l^{\text{nonRes}}\gamma'')^{-1}|^{-2} \times |v_{l-1} + v_{l-1}^{-1}\gamma''(i\gamma\kappa\tau_l\rho_l)^{-1}|^{-2}. \quad (39)$$

For the mode damping much lower than the coupling strength $|v_{l-1}^2| \gg \gamma''$ in low-loss structures, an approximate expression for the maximum FE in the resonator is found as

$$\text{FE}^{(4)}(\gamma') = |\tau_{l-1,l}/\eta_{l-1}|^2 = |\tau_{l-1}\rho_l^{-1}\mu_{l-1}^{-1}|^2 |v_{l-1}|^{-2}, \quad (40)$$

which describes the exponential growth of FE with the increasing thickness d_{l-1} of the spacer layer L_{l-1} in the ATR geometry.

From the expression (38), we can write the condition for the optimum coupling strength that provides a maximum

value of the resonator FE for a nonzero γ'' as

$$\text{Im}(\gamma\kappa P) = \gamma''. \quad (41)$$

The relation (41) defines the critical coupling conditions, i.e., when the intrinsic damping of the mode is equal to the recycled radiation gain; the radiation gain is determined by the component which outcouples to the radiation field and returns back to the resonator after multiple reflections. Assuming $\sigma_{l-1} = 1 - \mu_{l-1}r_{l-1,l}$, an analytical expression for an approximate optimum thickness d_{l-1}^{cc} , which gives a close-to-maximum value of the mode FE for a nonzero value of γ'' , can be derived from Eq. (39) for $\gamma' \gg \gamma''$ as

$$d_{l-1}^{\text{cc}} = \text{Re} \left\{ \frac{1}{4ik_0\beta_{l-1}} \left[i2\pi m + \ln \frac{\gamma''}{\text{Im}(\gamma\kappa\rho_l\tau_l r_{l-1,l-2})} \right] \right\}, \quad m \in \quad (42)$$

The relation (42) suggests different behaviors of d_{l-1}^{cc} depending on the excitation regime. In the case of guided modes excited under ATR conditions, i.e., WG modes, d_{l-1}^{cc} decreases logarithmically as γ'' increases. In the case of leaky modes, i.e., Fabry-Pérot modes, d_{l-1}^{cc} takes multiple values corresponding to the constructive interference in the structure.

It is worth mentioning that obtaining the analytical expressions for resonance properties, which characterize fields inside the resonance interference structures, e.g., maximum FE in the resonator and optimum thickness d_{l-1}^{cc} of the coupling layer, became possible only by using the developed spatial CMT.

Solving Eq. (35), we derive the following approximation of the total reflection coefficient $\tilde{r}_{l-2,l+1}$ in the same form as Eq. (23) obtained by the EM theory:

$$\tilde{r}_{l-2,l+1}(\alpha) = r_{l-2,l+1}^{\text{nonRes}} \frac{\alpha - \gamma[1 - \kappa(P r_{l-2,l-1} + \rho_{l,l-1}\Psi_0^{(4)})/r_{l-2,l+1}^{\text{nonRes}}]}{\alpha - \gamma(1 - \kappa P)}, \quad (43)$$

where $r_{l-2,l+1}^{\text{nonRes}} = r_{l-2,l-1} + (\rho_{l-1}/\tau_l + \rho_{l,l-1}\chi_l^{\text{nonRes}})\Psi_0^{(4)}$ is the amplitude of the nonresonance component as a function of the transfer coefficients. Applying some algebra, we arrive at the same expressions for the coefficients introduced for the EM case and conclude that the coincidence of the Fano expression (43) obtained by the CM model for the four-layer system with the Fano expression (23) demonstrates the correctness of the proposed CM model. In contrast to the CM model developed for SPP, the CM model described by Eqs. (32)–(35) takes into account the influence of the nonresonance back-reflections in the layer L_{l-1} to the nonresonance component $r_{l-2,l+1}^{\text{nonRes}}$ and to the changes in zero and pole values.

In our CM model, η_{l-1} , $\rho_{l,l-1}$, P , $\Psi_0^{(4)}$, and W depend on the outcoupling coefficient ρ_l and also exhibit resonance behavior. The ‘‘UFano’’ and ‘‘Fano’’ approaches can be again realized by considering ρ_l as a function of α and as a constant, respectively, as it was done in the three-layer case. In the EM theory, we can obtain modified Fano

expressions for the field amplitudes in four-layer systems assuming the resonance behavior of the coefficients $a(\alpha) = -(1 + r_{l-1,l}^{-1})[1 - \tilde{\sigma}_l(\alpha)]A_{l-1}$ and $b(\alpha) = -(1 + r_{l-1,l}^{-1})[1 - \tilde{\sigma}_l(\alpha)]C_{l-1}$ in Eqs. (22)–(24).

According to Eq. (43), for low-loss structures the shift in the real part of zero parameter, which determines the resonance position, is proportional to P , μ_{l-1} , η_{l-1} , and, therefore, proportional to the squared transfer coefficient v_{l-1}^2 . Under the ATR conditions, the lower self-coupling strength η_{l-1} , which is associated with thicker spacer layer L_{l-1} and higher in-plane mode propagation constants, results in lower resonance shifts. In the case of the excitation of radiative modes, the resonance position in spectra exhibits a sinusoidal dependence on d_{l-1} .

In the four-layer case, based on the 2×2 transfer matrix formalism and Fano approximations the coefficients of the CM model (33)–(35) are expressed as simple functions of transmission, reflection, and field transfer coefficients. We again demonstrated that to describe the interference phenomena in the resonator the CM coefficients should be considered as nonconstant.

C. System of coupled interference resonators

In this subsection, we further extend our CM model to the case of coupled interference resonators. We consider a six-layer system of $L_{l-2} - L_{l+3}$ layers constructed by a four-layer structure consisting of the $L_{l-2} - L_{l+1}$ layers considered in the previous subsection combined with a three-layer structure consisting of the $L_{l+1} - L_{l+3}$ layers. The three-layer $L_{l-1} - L_{l+1}$ stack in the four-layer structure can be regarded as the first resonator and the three-layer $L_{l+1} - L_{l+3}$ stack as the second resonator. These two interference resonators are separated by the spacer layer L_{l+1} .

Suppose that the resonators support interference modes with the mode excitation coefficients κ_1 and κ_2 and close propagation constants γ_1 and γ_2 , respectively. The coupling of the modes is mediated by the exponentially decaying waves in the spacer layer L_{l+1} . The total fields h_1 and h_2 in the first and second resonators can be represented as superpositions of the resonance and nonresonance components $h_1 = h_1^{\text{Res}} + h_1^{\text{nonRes}}$ and $h_2 = h_2^{\text{Res}} + h_2^{\text{nonRes}}$, respectively. Using the CMT formulations for the four-layer system, the following set of equations can be written for the resonance h_1^{Res} and nonresonance h_1^{nonRes} fields in the first resonator:

$$\begin{aligned} \frac{1}{ik_0\gamma_1} \frac{dh_1^{\text{Res}}}{dx} &= h_1^{\text{Res}} + \kappa_1 \tau_{l-1,l} h_{l-2,l-1} + \kappa_1 \eta_{l-1} (h_1^{\text{Res}} + h_1^{\text{nonRes}}) + \kappa_1 o_{21} h_{l+1}^-, \\ h_1^{\text{nonRes}} &= \chi_l^{\text{nonRes}} \tau_{l-1,l} h_{l-2,l-1} + \chi_l^{\text{nonRes}} \eta_{l-1} (h_1^{\text{Res}} + h_1^{\text{nonRes}}) + \chi_l^{\text{nonRes}} o_{21} h_{l+1}^-, \\ h_{l+1}^+ &= t_{l,l+1} (h_1^{\text{Res}} + h_1^{\text{nonRes}}), \end{aligned} \quad (44)$$

where h_{l+1}^+ is the field of the first resonator outcoupled to the second resonator, $o_{21} = (\xi_l + \zeta_l) t_{l+1,l} v_{l+1}$ is the total coupling coefficient of the field h_{l+1}^- outcoupled from the second resonator at the interface $I_{l+1,l+2}$ to that of the first resonator. The coefficient o_{21} is represented as a sum of the transfer coefficients for two paths with $\xi_l = v_l^2 r_{l,l-1}$ for the waves reflected from the interface $I_{l-1,l}$ to the interface $I_{l,l+1}$ in the layer L_l and $\zeta_l = v_l t_{l,l-1} v_{l-1}^2 r_{l-1,l-2} \tau_l \sigma_{l-1}^{-1}$ for the waves that pass the interface $I_{l-1,l}$, reflect from the interface $I_{l-2,l-1}$ to the interface $I_{l-1,l}$, undergo multiple reflections in the layer L_{l-1} , and pass to the interface $I_{l,l+1}$ in the layer L_l .

The field in the second resonator with the semi-infinite layer L_{l+3} is obtained using the three-layer CM model described by Eqs. (25)–(27) as follows:

$$\begin{aligned} \frac{1}{ik_0\gamma_2} \frac{dh_2^{\text{Res}}}{dx} &= h_2^{\text{Res}} + \kappa_2 \eta_{l+1} (h_2^{\text{Res}} + h_2^{\text{nonRes}}) + \kappa_2 o_{12} h_{l+1}^+, \\ h_2^{\text{nonRes}} &= \chi_{l+2}^{\text{nonRes}} \eta_{l+1} (h_2^{\text{Res}} + h_2^{\text{nonRes}}) + \chi_{l+2}^{\text{nonRes}} o_{12} h_{l+1}^+, \\ h_{l+1}^- &= r_{l+1,l+2} v_{l+1} h_{l+1}^+ + \rho_{l+2} (h_2^{\text{Res}} + h_2^{\text{nonRes}}), \end{aligned} \quad (45)$$

where $o_{12} = \tau_{l+2} v_{l+1}$ is the coefficient describing the coupling of field of the first resonator to that of the second resonator.

In what follows, we assume that the positions of the resonances of the first and second resonators are close, i.e., the resonances are characterized by the propagation constants γ_1 and γ_2 with real parts close to each other ($\gamma_1' \cong \gamma_2'$). In the vicinity of both resonances $\alpha \rightarrow \gamma_1', \gamma_2'$, the dependencies of the amplitudes of fields $h_1 = h_1^{\text{Res}} + h_1^{\text{nonRes}}$ and $h_2 = h_2^{\text{Res}} + h_2^{\text{nonRes}}$ in the first and second resonators, respectively, on α are found as

$$\begin{aligned} \frac{h_1}{h_{l-2,l-1}} &= \frac{\tau_{l-1,l}}{\frac{(1 - \chi_l^{\text{nonRes}} \eta_{l-1})(\alpha - \gamma_1) - \gamma_1 \kappa_1 \eta_{l-1}}{\chi_l^{\text{nonRes}} (\alpha - \gamma_1) + \gamma_1 \kappa_1} - \frac{[\chi_{l+2}^{\text{nonRes}} (\alpha - \gamma_2) + \gamma_2 \kappa_2] \rho_{l+2} o_{12} o_{21} t_{l,l+1}}{(1 - \chi_{l+2}^{\text{nonRes}} \eta_{l+1})(\alpha - \gamma_2) - \gamma_2 \kappa_2 \eta_{l+1}} - r_{l+1,l+2} o_{21} \tau_{l+1}}, \\ \frac{h_2}{h_{l-2,l-1}} &= \frac{\frac{\chi_{l+2}^{\text{nonRes}} (\alpha - \gamma_2) + \gamma_2 \kappa_2}{(1 - \chi_{l+2}^{\text{nonRes}} \eta_{l+1})(\alpha - \gamma_2) - \gamma_2 \kappa_2 \eta_{l+1}} \tau_{l+2} \tau_{l+1} \tau_{l-1,l}}{\frac{(1 - \chi_l^{\text{nonRes}} \eta_{l-1})(\alpha - \gamma_1) - \gamma_1 \kappa_1 \eta_{l-1}}{\chi_l^{\text{nonRes}} (\alpha - \gamma_1) + \gamma_1 \kappa_1} - \frac{[\chi_{l+2}^{\text{nonRes}} (\alpha - \gamma_2) + \gamma_2 \kappa_2] \rho_{l+2} o_{12} o_{21} t_{l,l+1}}{(1 - \chi_{l+2}^{\text{nonRes}} \eta_{l+1})(\alpha - \gamma_2) - \gamma_2 \kappa_2 \eta_{l+1}} - r_{l+1,l+2} o_{21} \tau_{l+1}}}. \end{aligned} \quad (46)$$

The expressions (46) describe the amplitude enhancements in the system of the two coupled optical resonators, when the responses of the resonators include both the resonance and nonresonance components. The contribution of the nonresonance component is determined by the coefficients χ_l^{nonRes} and $\chi_{l+2}^{\text{nonRes}}$. For small nonresonance components, $\chi_l^{\text{nonRes}}, \chi_{l+2}^{\text{nonRes}} \rightarrow 0$, the total field is represented by the resonance component, and the following expressions can be obtained from the relations (46):

$$\begin{aligned} \frac{h_1}{h_{l-2,l-1}} &= \frac{[\alpha - \gamma_2 (1 + \kappa_2 \eta_3)] \tau_{l-1,l} \gamma_1 \kappa_1}{\{\alpha - \gamma_1 [1 + \kappa_1 (\eta_1 + r_{l+1,l+2} o_{21} \tau_{l+1})]\} [\alpha - \gamma_2 (1 + \kappa_2 \eta_3)] - \rho_{l+2} o_{21} o_{12} t_{l,l+1} \gamma_1 \kappa_1 \gamma_2 \kappa_2}, \\ \frac{h_2}{h_{l-2,l-1}} &= \frac{\tau_{l+2} \tau_{l+1} \tau_{l-1,l} \gamma_1 \kappa_1 \gamma_2 \kappa_2}{\{\alpha - \gamma_1 [1 + \kappa_1 (\eta_1 + r_{l+1,l+2} o_{21} \tau_{l+1})]\} [\alpha - \gamma_2 (1 + \kappa_2 \eta_3)] - \rho_{l+2} o_{12} o_{21} t_{l,l+1} \gamma_1 \kappa_1 \gamma_2 \kappa_2}. \end{aligned} \quad (47)$$

We note here that the Fano form of Eqs. (47) coincides with the form of equations derived for a system of two coupled mechanical oscillators [30,31], which describe excitation of the resonance components only.

TABLE I. Structural parameters of the samples.

Layer no.	3LWG			4LWG			4LMWG		
	d (nm)	n	κ	d (nm)	n	κ	d (nm)	n	κ
0	–	–	–	–	1.5	0	–	1.5	0
1	–	1.0	0	800	1.0	0	25	0.13231	6.9045
2	300	1.5	1×10^{-4}	300	1.5	1×10^{-4}	450	1.5	1×10^{-4}
3	–	1.0	0	–	1.0	0	–	1.0	0
Layer no.	4LFP			6L2FP					
	d (nm)	n	κ	d (nm)	n	κ			
0	–	1.0	0	–	1.0	0			
1	10	0.13231	6.9045	13	0.13231	6.9045			
2	3000	1.5	0	700	1.5	0.02			
3	–	0.13231	6.9045	40	0.13231	6.9045			
4	–	–	–	3000	1.5	0			
5	–	–	–	–	0.13231	6.9045			

As in the case of the system of two coupled mechanical oscillators, the response of the optical system (46) is characterized by the same denominator. The propagation constants of the normal modes of the coupled system are found from the condition that the denominator is equal to zero. Based on the coupling regime the coupled modes are characterized by the symmetric and antisymmetric compositions of fields of the uncoupled modes. The relation (46) suggests that the coefficients of the nonresonance component excitation as well as the self-coupling coefficients of the resonator fields affect the position and the line shape of the resonances.

In the coupled system, the backward field h_{l-2}^- at the interface $I_{l-2,l-1}$ includes a component of the field directly outcoupled from the second resonator in addition to that from the first resonator

$$h_{l-2}^- = r_{l-2,l-1} h_{l-2,l-1} + \rho_{l,l-1} (h_1^{\text{Res}} + h_1^{\text{nonRes}}) + \rho_{l-1} h_{l-1,l} + \delta h_{l+1}^-, \quad (48)$$

where $\delta = v_{l+1} t_{l+1,l} v_l t_{l,l-1} v_{l-1} t_{l-1,l-2}$ is an outcoupling coefficient. Substituting Eq. (32) and the expression for h_{l+1}^- obtained from Eqs. (44) and (45) to the expression (48) for the backward field h_{l-2}^- , the total reflection coefficient $\tilde{r}_{l-2,l+3}$ of the five-layer structure is found as a superposition

$$\tilde{r}_{l-2,l+3} = r_{l-2,l+3}^{\text{nonRes}} + (\rho_{l,l-1} + \eta_{l-1} \rho_{l-1} / \tau_l + \delta r_{l+1,l+2} \tau_{l+1}) h_1 / h_{l-2,l-1} + \delta \rho_{l+2} h_2 / h_{l-2,l-1}, \quad (49)$$

where $r_{l-2,l+3}^{\text{nonRes}} = r_{l-2,l-1} + \rho_{l-1} \tau_{l-1,l} / \tau_l$ is a nonresonance component of the reflection coefficient. The expression (49) demonstrates that the resonances in total reflectivity spectra $|\tilde{r}_{l-2,l+3}(\alpha)|^2$ of the coupled interference resonator systems are characterized by asymmetric line shapes as a result of Fano interference of the fields generated by both resonance subsystems and the nonresonance reflections.

IV. VALIDATION OF NUMERICAL RESULTS

In the previous subsection, we developed CM models that bring the same Fano expressions as those obtained by the ap-

proximations within the EM theory. In this section, to explore the reliability of the proposed CM models we compare numerical results obtained by the Fano approximations based on constant and variable coefficients, i.e., ‘‘Fano’’ and ‘‘UFano’’ approximations, with those of rigorous EM theory for several different cases of resonant mode excitations in planar interference resonators.

Let us consider five different multilayer structures denoted as 3LWG, 4LWG, 4LMWG, 4LFP, and 6L2FP. These structures are chosen to cover different modes excited in the multilayer structure. The three-layer low-loss dielectric 3LWG structure is a fundamental structure that supports a WG mode with a small attenuation. The four-layer low-loss dielectric 4LWG structure is the ATR configuration with the 3LWG structure. The 4LMWG structure is the ATR configuration like the 4LWG structure with high loss induced by a thin metal spacer layer. The four-layer 4LFP structure is an MIM structure supporting Fabry-Pérot modes. The six-layer 6L2FP structure is an MIMIM structure that supports two Fabry-Pérot modes coupled to each other. The geometrical and optical parameters (thickness d , refractive index n and extinction coefficient κ of each layer) characterizing all structures are summarized in Table I.

Reflectivity spectra were calculated rigorously for each sample. The exact reflectivity spectra were approximated by ‘‘Fano’’ and ‘‘UFano’’ approaches. In the calculations, we assumed the incidence of s - and p -polarized plane waves with $\lambda = 1000$ nm on the multilayer sample from the layer L_0 . The refractive index of metal layers corresponds to data of gold taken from [59].

Appendix B describes the following parameters important for the validation section. The parameters of the ‘‘Fano’’ and ‘‘UFano’’ approximations with the resonance characteristics, and the CM parameters are presented for the one-mode structures in Tables II and III, respectively.

A. An absorptive WG with semi-infinite dielectric claddings

To estimate the error of the Fano approximation and the corresponding CM model for three-layer structures, we

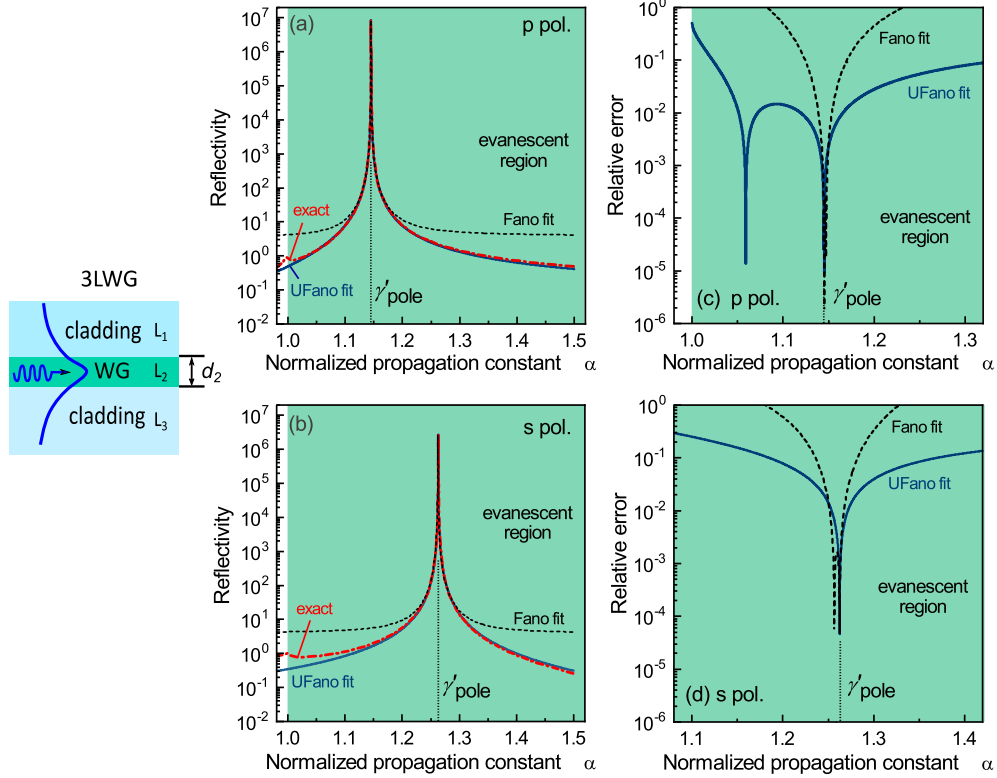


FIG. 4. Three-layer dielectric WG structure (3LWG structure). Comparison of the exact solution $|r_{1,3}|^2$ (red dashed line) with the “Fano” $|\tilde{r}_{1,3}|^2$ [Eq. (21) or (28)] (black dashed line) and “UFano” $|\hat{r}_{1,3}|^2$ [Eq. (30)] (blue solid curve) approaches for (a) p -polarized and (b) s -polarized excitations. The relative error of the “Fano” (black dashed line) and “UFano” (blue solid line) approximations for (c) p -polarized and (d) s -polarized excitations. The filled areas correspond to the evanescent region.

consider a 3LWG structure that consists of a low-loss high-index waveguide layer with a thickness of 300 nm sandwiched between two semi-infinite low-index clads with the refractive index $n = 1.0$. The structure is schematically shown in Fig. 4. We study the optical properties of the structure by varying the normalized in-plane propagation constant α in a range from 0 to 1.5 refractive index units (RIU) at $\lambda_0 = 1000$ nm.

The complex effective refractive indices γ of the WG modes supported by the structure were obtained using the approach described in Ref. [51]. As γ values are higher than the refractive indices of clads, the WG modes can be excited by evanescent plane waves. Positions of the resonances are determined by the real parts of the pole parameter, which equals to the mode effective index. The exact reflectivity spectra $|r_{1,3}^{(3)}|^2$ were calculated based on the 2×2 transfer matrix approach described in Appendix A for both the p and s polarizations. The reflectivity spectra as functions of α presented in Figs. 4(a) and 4(b) exhibit very sharp asymmetric resonances in the evanescent region near $\alpha = \gamma'_{\text{pole}} = \gamma'$. These resonances with the resonance peaks of 9.293985×10^6 and 2.979241×10^6 are associated with the excitation of TM_0 and TE_0 WG modes for p and s polarizations, respectively.

To confirm the correctness of the approximate expressions (21) and (30), we calculated reflectivity spectra $|\tilde{r}_{1,3}|^2$ (“Fano”) and $|\hat{r}_{1,3}^{(3)}|^2$ (“UFano”) in the evanescent region and the results are shown in Figs. 4(a) and 4(b). The figures demonstrate that the “Fano” result shows an overall good

agreement with the exact data in a narrow region of $\gamma' \pm 0.05$ RIU, whereas the “UFano” approximation coincides with the exact data in a much broader region.

Using the analytical expression (19), we estimated the maximum FE in the middle layer of the order of 10^7 as summarized in Table II. According to Eq. (19) the maximum FE is mainly driven by the inverse proportionality to γ'^2 that provides a ~ 4 times higher value in the case of p polarization as compared to that of s polarization.

The maximum FE values of the reflected field $|\hat{r}_{1,3}|_{\text{max}}^2$ were estimated using Eq. (31). Furthermore, the approximate values of the resonance FWHM were estimated using Eq. (7). From the obtained values we found that the relative error of the “UFano” approximation in the resonance vicinity is less than $6 \times 10^{-3}\%$.

Based on the estimations of pole and zero parameters, we determined the values of the normalized amplitude of resonance component q by Eq. (5) and the asymmetry parameter \bar{q} of the generalized Fano function (8). As shown in Table II, for both polarizations $|q''| \gg |q'|$ and $\arg(q)$ is close to $-\pi/2$ that defines the resonance line shape as symmetric.

To quantitatively estimate the divergence of these approximations from the exact solution in the evanescent region, we calculated the relative errors for the “Fano” $||r_{1,3}|^2 - |\tilde{r}_{1,3}|^2|/|r_{1,3}|^2$ and “UFano” $||r_{1,3}|^2 - |\hat{r}_{1,3}|^2|/|r_{1,3}|^2$ approximations as functions of α . The results calculated for p and s polarizations are shown in Figs. 4(c) and 4(d), respectively.

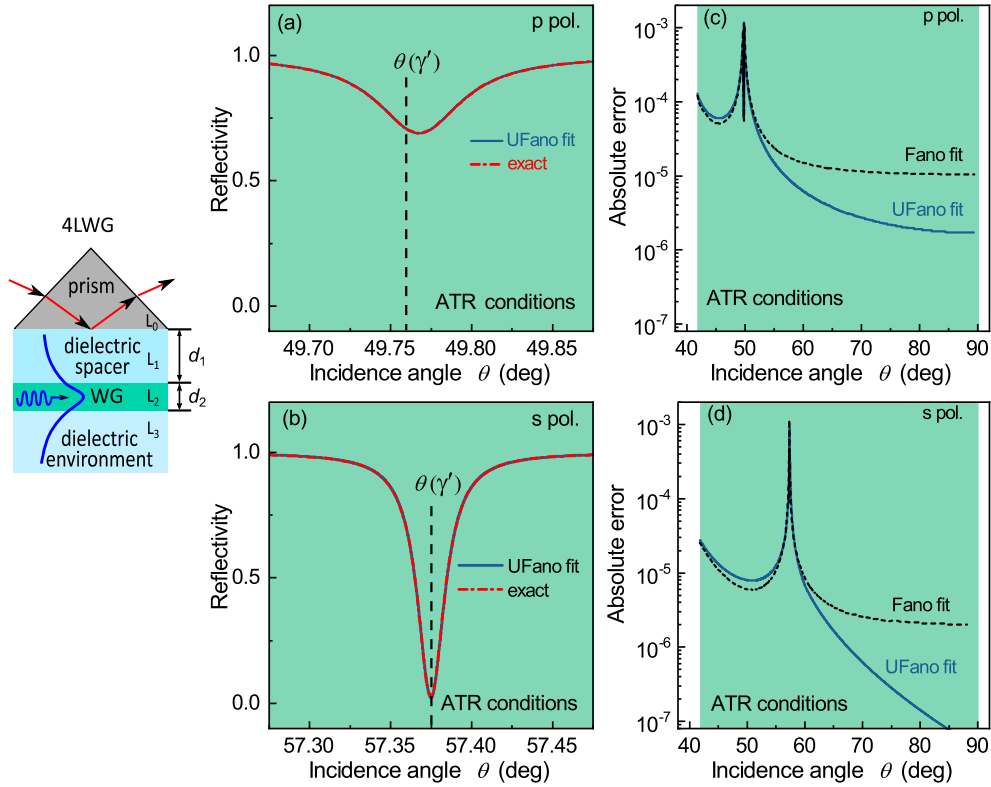


FIG. 5. Four-layer dielectric WG structure in the ATR geometry (4LWG structure). Comparison of the exact solution $|r_{0,3}|^2$ (red bold dots) with the approximated data $|\tilde{r}_{0,3}|^2$ using the “UFano” (blue solid line) approach for (a) p -polarized and (b) s -polarized excitations. The absolute error of the “Fano” (black dashed line) and “UFano” (blue solid line) approximations for (c) p -polarized and (d) s -polarized excitations. The filled areas correspond to the evanescent region.

As can be seen from the figures, in the resonance vicinity $\alpha = \gamma'_{\text{pole}}$, the relative error is minimal for both the “Fano” and “UFano” approximations. In the case of p polarization, the relative error of less than 2% is achieved in the regions with width of 0.14 RIU and 0.2 RIU for the “Fano” and “UFano” approximations, respectively. In the case of s polarization, the width of regions of the 2% margin is narrower: 0.02 RIU and 0.04 RIU for the “Fano” and “UFano” approximations, respectively. Moreover, the relative error of the “UFano” approximation is less than 10% in much wider widths of 0.32 and 0.1 RIU for p and s polarizations, respectively. Therefore, the fact that the numerical results obtained by the CM model are in excellent agreement with the exact data near and beyond the resonance vicinity demonstrates the validity of our CM models.

B. An absorptive WG with dielectric claddings in the ATR configuration

In the next subsections, we focus on the error of the Fano approximation and corresponding CM model for four-layer structures and examine a 4LWG system that is constructed by adding a dielectric layer (L_0 layer) with a high refractive index to the 3LWG structure considered above. The structure is schematically shown in Fig. 5. This system can be regarded as an ATR configuration, in which a high-index low-loss WG layer is separated from a high-index prism by a low-index

dielectric spacer layer. Plane waves propagating in the high-index layer L_0 generate evanescent waves in the L_1 layer that excite the WG modes in the layer L_2 under ATR conditions. To choose the thickness d_1 of the layer L_1 we estimated the thicknesses d_1^{cc} of the dielectric layer L_1 providing the critical coupling condition and maximum mode FE for the 4LWG structure by Eq. (42) as 1139.9 nm and 768.0 nm for p and s polarizations, respectively. Further, we fix the thickness d_1 of the layer L_1 at 800 nm, which is close to d_1^{cc} for s polarization, that generates symmetric line shapes in the calculation results for both polarizations.

The exact ATR spectra $|r_{0,3}|^2$ were calculated by the 2×2 transfer matrix described in Appendix A for both the p and s polarizations. The ATR spectra are shown in Figs. 5(a) and 5(b) as functions of the incidence angle $\theta(\alpha) = \arcsin(\alpha/n_0)$ of the exciting wave. The resonance dips with the minimum values R_{min} seen in the figures at the resonance angles θ_{res} are associated with the excitation of TM_0 and TE_0 WG modes for p and s polarizations, respectively. The line shapes of the resonances are symmetric for both polarizations.

The approximate ATR spectra $|\tilde{r}_{0,3}|^2$ were calculated by Eq. (43) using “Fano” and “UFano” approaches. Since the spectra resulting from two approximations are close to each other, only the “UFano” results are compared with the exact data in Figs. 5(a) and 5(b). The figures demonstrate excellent agreement of the approximations to the exact data in the whole ATR region.

The maximum FE in the WG layer L_2 are calculated by Eq. (39) and presented in Table II. The excitation of the TE_0 WG mode leads to a value (2350.7) higher than that achieved by the excitation of the TM_0 WG mode (272.5), by approximately an order of magnitude. Besides that, the resonance is narrower in the case of s polarization. The imaginary part of the complex effective refractive index γ'' of the TE_0 WG mode is almost ~ 2 times higher than that of the TM_0 WG mode (see Table II). Therefore, the behavior of the resonances in the four-layer structures cannot be explained by the behavior of γ'' values of the three-layer WG modes.

Due to the multiple reflections in the adjacent layers and mode self-coupling, the resonances determined by the pole parameters of the four-layer structures γ_{pole} are shifted from the positions of the effective refractive indices of three-layer modes. The maximum $FE^{(4)}$ can be estimated more exactly using the general Fano formula (6) and Eq. (38) at $\alpha = \gamma'_{\text{pole}}$ as $FE^{(4)}(\gamma'_{\text{pole}}) = |\Psi_0^{(4)} \chi_l^{\text{nonRes}}|^2 [(\gamma'_{\text{pole}} - \gamma'_{\text{zero}})^2 + \gamma''_{\text{zero}}] / \gamma''_{\text{pole}}$. As $FE^{(4)}$ is inversely proportional to γ''_{pole} , the higher maximum FE in the TE_0 case results from the lower imaginary part of the TE_0 pole (see Table II). Eq. (39) is helpful to clarify the origins of the difference in FE values for TE_0 and TM_0 cases. In fact, Eq. (39) suggests that for $|\nu_{l-1}| \gg \gamma''$ the FE lower limit is inversely proportional to the squared module of transfer coefficient ν_{l-1} . We can conclude that the higher FE value is achieved in the s polarization case due to a higher mode effective index and a lower transfer coefficient as compared to those of the p polarization case. The resonance FWHM is proportional to γ''_{pole} as suggested by Eq. (7), and the ~ 3 times wider FWHM in the p polarization case results from the ~ 3 times higher γ''_{pole} as compared to those of s polarization case (see Table II).

The real parts of the zero and pole parameters take nearly the same values for both the s and p polarizations (see Table II). This fact leads to $\arg(q)$ values close to $-\pi/2$ that classify the resonance spectra into symmetric line shapes as can be seen in Figs. 5(a) and 5(b).

According to Eq. (24), the real part of γ_{zero} determines the position of a resonance dip. In the case of p polarization, the real part of γ_{zero} is higher than γ' by $\sim 1.1 \times 10^{-4}$ RIU. The difference for the s polarization case is lower and has an opposite sign: -2.8×10^{-6} RIU. These differences are manifested in the shifts of the resonance positions of the ATR spectra of $+0.0078^\circ$ and -0.0002° from the resonance positions of the TE_0 and TM_0 WG modes in the three-layer structure, respectively. The higher resonance shift in the p polarization case is originated from the higher back-coupling coefficient P , which is proportional to the self-coupling coefficient η and the coefficient of back-reflection η_{l-1} , which are proportional to the squared transfer coefficient. The stronger self-coupling and back-reflection in the p polarization case is a result of the lower mode effective index as compared to that of the s polarization. Therefore, a higher shift of the resonance position is accompanied by a lower FE of the mode.

The absolute errors $||r_{0,3}|^2 - |\tilde{r}_{0,3}|^2|$ for the “Fano” and “UFano” approximations were estimated as functions of θ in the ATR region and shown in Figs. 5(c) and 5(d). The absolute errors are close for both the “Fano” and “UFano” approximations achieving the maximum values of $\sim 10^{-3}$ in

the resonance vicinity. In the region of $\theta(\alpha) > \theta(\gamma')$, the “UFano” absolute error takes lower values as compared to that of the “Fano” approximation. We conclude that the numerical results obtained by the CM model in the four-layer case are also in excellent agreement with the exact data, and the “Fano” approximations is as accurate as the “UFano” approximation.

C. An absorptive WG with a metallic spacer layer in the ATR configuration

Another planar structure considered here consists of a high-index dielectric low-loss WG layer 450 nm in thickness separated from a high-index prism by a thin gold film. This is a four-layer system denoted as 4LMWG structure with the parameters given in Table I. The WG modes in the structure are also excited under the ATR conditions and characterized by attenuation higher than that of the modes in the 4LWG structure. According to Eq. (42) the values of critical coupling thickness d_1^{cc} of the gold layer L_1 in the 4LMWG structure are 45.2 nm and 33.5 nm for p and s polarizations, respectively. The ATR spectra of the structure with d_1^{cc} show deep and sharp resonances with nearly symmetric line shapes. In the following, we consider the structure with a thickness d_1 of 25 nm, which is smaller than d_1^{cc} and characterized by higher mode self-coupling strength, to increase the shift of resonance position from that of the three-layer WG mode. The exact ATR spectra of the structure are given in Figs. 6(a) and 6(b).

In the absence of the WG layer, the resonance corresponding to the excitation of SPP at the gold-air interface is located at $\theta = 42.6^\circ$. In the presence of the WG layer, the SPP resonance shifts to higher angles as the WG layer thickness increases due to the SPP mode self-coupling by back reflections in the adjacent layers [15]. At the thickness of 450 nm the SPP mode is located at $\theta = 85.5^\circ$ and does not appear in the presented ATR spectra.

In the figures, we see asymmetric resonance dips associated with the excitation of the TM_0 and TE_0 WG modes. The shifts of the resonance positions from those of the three-layer metal-WG-insulator structure are higher as compared to the shifts in the spectra of the previous structures (3LWG, 4LWG) with lower losses found in Figs. 4 and 5. The numerical results obtained from the “Fano” and “UFano” approximations are shown in Figs. 6(a) and 6(b), respectively. We can see an excellent agreement between the “UFano” approximation and the exact calculation in a broad angular region and a good agreement of the “Fano” approximation in a narrow region near the resonance vicinity $\alpha \rightarrow \gamma'$.

To characterize the resonance line shapes in the ATR spectra, we calculated the values of zero and pole parameters of the expression (24) for the p and s polarizations and listed them in Table II. In both cases, $|q|$ is close to 1.0 and $\arg(q)$ of -0.40235π for the p polarization and -0.43926π for the s polarization, are not close to $\pm\pi/2$, making the resonance line shapes more asymmetric as compared to those of the WG structure with dielectric claddings. Note that as the real part of q increases, $\arg(q)$ approaches zero, and the line shape becomes asymmetric. According to Eq. (24), $q = \gamma_{\text{pole}} - \gamma_{\text{zero}}$ is proportional to the mode excitation coefficient κ determined by Eq. (12). For the low-loss structures the module of the real part of κ is smaller than the module of the imaginary part. The

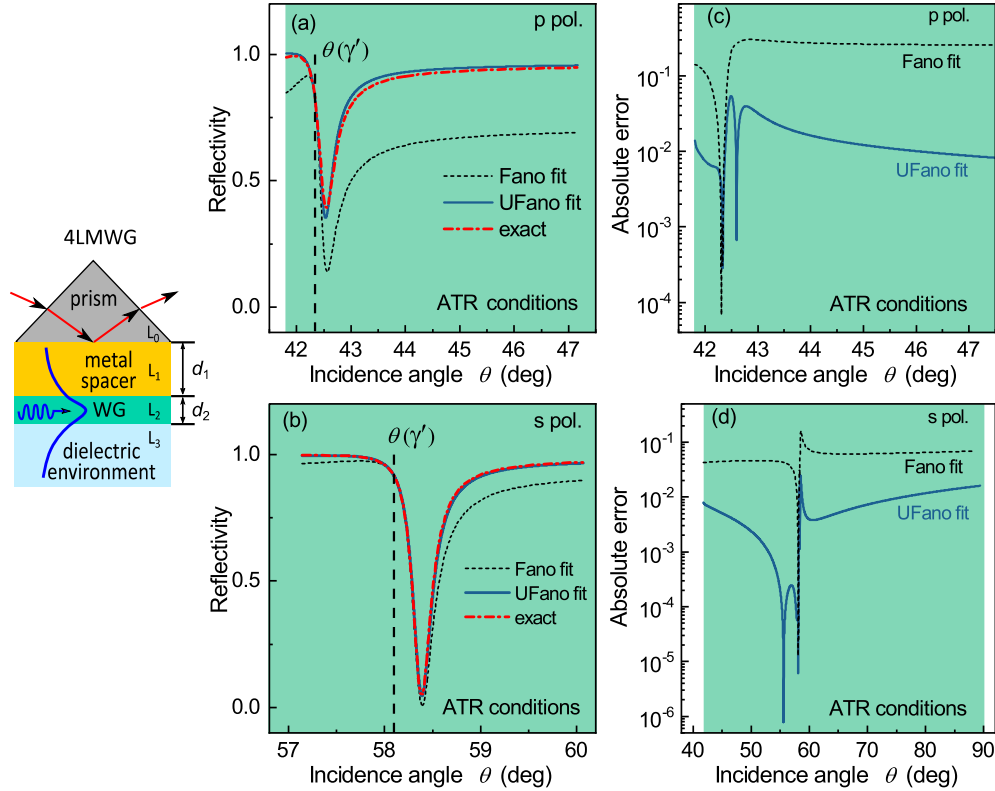


FIG. 6. Four-layer WG structure with a metallic cladding in the ATR geometry (4LMWG structure). Comparison of the exact solution $|r_{0,3}|^2$ (red bold dots) with the “UFano” (blue solid line) and “Fano” (black dashed line) $|\tilde{r}_{0,3}|^2$ approximations for (a) p -polarized and (b) s -polarized excitations. The absolute error of the approximations for (c) p -polarized and (d) s -polarized excitations. The filled areas correspond to the evanescent region.

resonance component is, therefore, characterized by a phase shift of $\pm\pi/2$ relative to the nonresonance component that results in the symmetric resonances. Losses imposed to the structure increase the real part of κ and q moving the phase shift towards to zero that leads to asymmetric resonances. An absorption in the metal layer L_1 in the 4LMWG structure thus results in the real part of κ higher by an order of magnitude as compared to that of the 4LWG structure with loss-less dielectric layer L_1 as found in Table II. The increased absorption in the 4LMWG structure also leads to higher values of γ''_{pole} and FWHM as compared to the 4LWG structure.

Due to thinner layer L_1 in the 4LMWG structure, the coefficients of self-coupling η_1 and back-coupling P are higher by an order of magnitude than those of the 4LWG structure as can be seen from Tables B2 and B3. According to Eq. (43), this implies larger shifts of the three-layer modes and lower FE of the modes in the 4LMWG structure as found in the Table II.

The absolute errors for the “Fano” and “UFano” approximations are shown in Figs. 6(c) and 6(d) as functions of θ in the ATR region. The “UFano” absolute error does not exceed 0.055 and 0.025 for p and s polarizations, respectively. The “Fano” results exhibit much higher divergence and take low error values in the narrow resonance region of $\theta(\gamma') \pm 0.25^\circ$.

D. An absorptive Fabry-Pérot MIM structure

In this subsection, we consider a four-layer structure, denoted as 4LFP structure, containing an MIM structure. The

MIM structure consists of a $3\text{-}\mu\text{m}$ -thick high-index loss-less dielectric layer sandwiched between a semi-infinite gold substrate and a thin gold film. This structure supports Fabry-Pérot modes, and the modes can be excited by a plane wave incident from air at the thin gold film side. The critical coupling thicknesses d_1^{cc} of the thin gold layer calculated by Eq. (42) are 35.1 nm and 27.5 nm for p and s polarizations, respectively. To enhance the asymmetry of the Fabry-Pérot resonances, we selected a thickness of 10 nm, which is smaller than d_1^{cc} and provides higher self-coupling strength of the resonator field.

To generate the asymmetric resonances in angular spectra of the MIM structure we selected eighth-order radiative Fabry-Pérot modes with complex effective refractive indices γ of $0.735539 + i8.79 \times 10^{-4}$ RIU and $0.724375 + i6.56 \times 10^{-4}$ RIU for p and s polarizations, respectively. The exact reflectivity spectra of the structure are compared with the Fano approximations in Figs. 7(a) and 7(b). To focus on the excitation of these Fabry-Pérot modes, the angle of incidence θ is scanned in the radiative region only. The spectra exhibit asymmetric resonance dips for both polarizations.

We see that the exact reflectivity spectra are very well reproduced by the “UFano” approximation in a wide angular region, whereas the “Fano” results just partly approximate the exact solutions in narrower regions near $\alpha = \gamma'$. The estimates of maximum FE in the dielectric layer take much lower values as compared to the 4LWG and 4LMWG structures due to higher absorption in the metal layers.

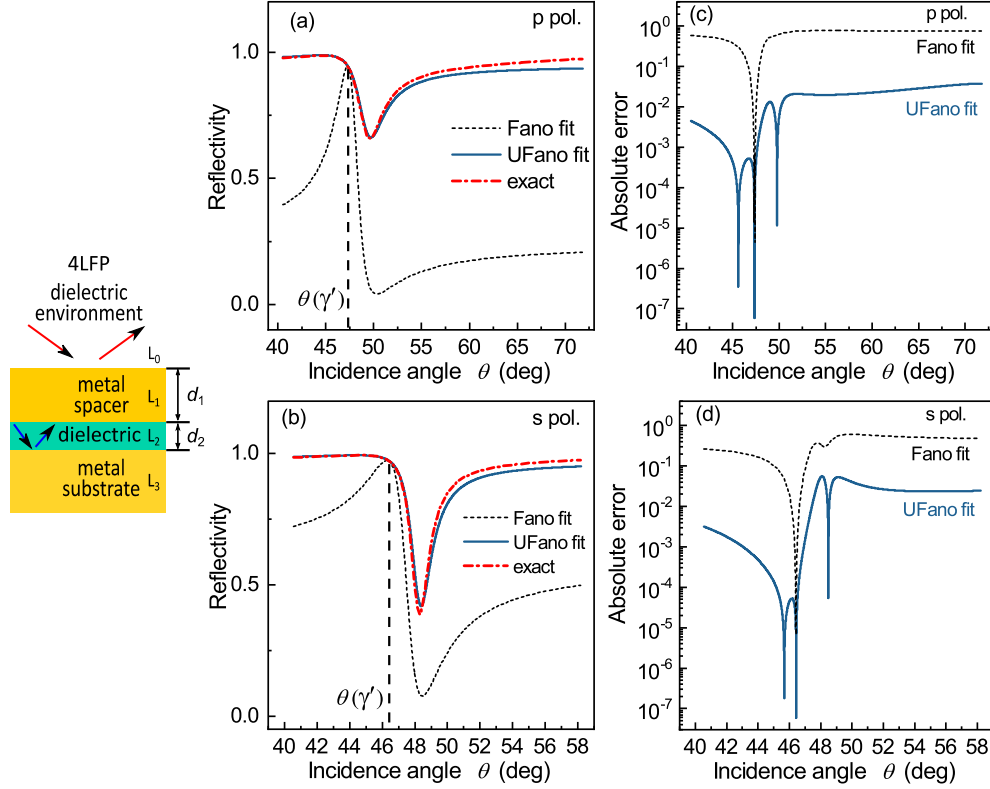


FIG. 7. Exact reflectivity spectra $|r_{0,3}|^2$ (red bold dots), and “UFano” (blue solid line) and “Fano” (black dashed line) approximations in the four-layer MIM structure, which support excitation of radiative Fabry-Pérot modes for (a) p and (b) s polarizations (4LFP structure). The absolute error of the approximations for (c) p and (d) s polarizations.

The values of the normalized amplitude of resonance component q were estimated based on the zero and pole parameters. For both polarizations, $|q|$ is close to 1.0 and $\arg(q)$ is around -0.2π . Since these $\arg(q)$ values are not close to $\pm\pi/2$, the asymmetric resonance line shapes are generated. As the thickness of the L_1 layer in the 4LFP structure is the thinnest among the considered structures, the 4LFP structure exhibits the strongest self-coupling (see Table III). As a result, in the 4LFP structure, the resonance shift is the highest, and the mode FE is the weakest.

The absolute errors of the “Fano” and “UFano” approximations are plotted in Figs. 7(c) and 7(d) as functions of θ . The “UFano” absolute error does not exceed 0.02 and 0.056 in the broad angular region of $\theta(\gamma') \pm 10^\circ$ for p and s polarizations, respectively. The “Fano” results show low error values in a much narrower range of $\theta(\gamma') \pm 0.35^\circ$.

E. Coupling of two Fabry-Pérot modes in a MIMIM structure

In this subsection, we consider a stack of two MIM structures denoted as 6L2FP structure. In the stack, the MIM structures are separated by the middle spacer metal layer as presented in Fig. 8. The composite reflective MIMIM structure consists of four finite-thickness layers: a stack of two gold layers L_1 and L_3 and two dielectric layers L_2 and L_4 placed on a semi-infinite gold substrate L_5 . The semi-infinite layer L_0 represents a dielectric environment. Both of the dielectric layers are sandwiched by the gold layers and they form the cores of two MIM Fabry-Pérot resonators. Here-

after, we denote these MIM structures as MIM1 ($L_1 - L_3$) and MIM2 ($L_3 - L_5$) resonators. The MIM2 resonator is the same as the MIM structure considered in the previous subsection and supports the same Fabry-Pérot mode with the propagation constant γ_2 of $0.735539 + i8.79 \times 10^{-4}$ RIU and $0.724375 + i6.56 \times 10^{-4}$ RIU for p and s polarizations, respectively. The MIM1 includes a lossy dielectric layer L_2 with the refractive index of $n_2 = 1.5 + i0.02$ and thickness of $d_2 = 700$ nm and supports excitation of second-order radiative Fabry-Pérot mode with the propagation constant γ_1 of $0.717942 + i0.051733$ RIU and $0.6720551 + i0.047555$ RIU for p and s polarizations, respectively. The modes of MIM1 are directly excited by an external light field. High intrinsic losses in the MIM1 resonator bring low- Q broad resonances, while MIM2 resonator provides sharp high- Q resonances.

The MIM1 and MIM2 structures are separated from each other by the gold spacer layer L_3 . When the layer L_3 is thin enough the modes can couple each other through the exponentially decaying waves propagating in the gold layer L_3 . The thicker layer L_3 results in the weaker mode coupling. To demonstrate the mode intercoupling that leads to the appearance of highly asymmetric resonance line shapes in the reflectivity spectra in a weak coupling regime, we fixed the thickness of the gold layer L_3 at $d_3 = 40$ nm.

The “Fano” and “UFano” approximations of the reflectivity spectra for the 6L2FP structure were obtained using Eq. (49) for constant and variable values of ρ_2 , ρ_4 , and o_{21} , respectively. The resonance behavior of o_{21} is assumed as

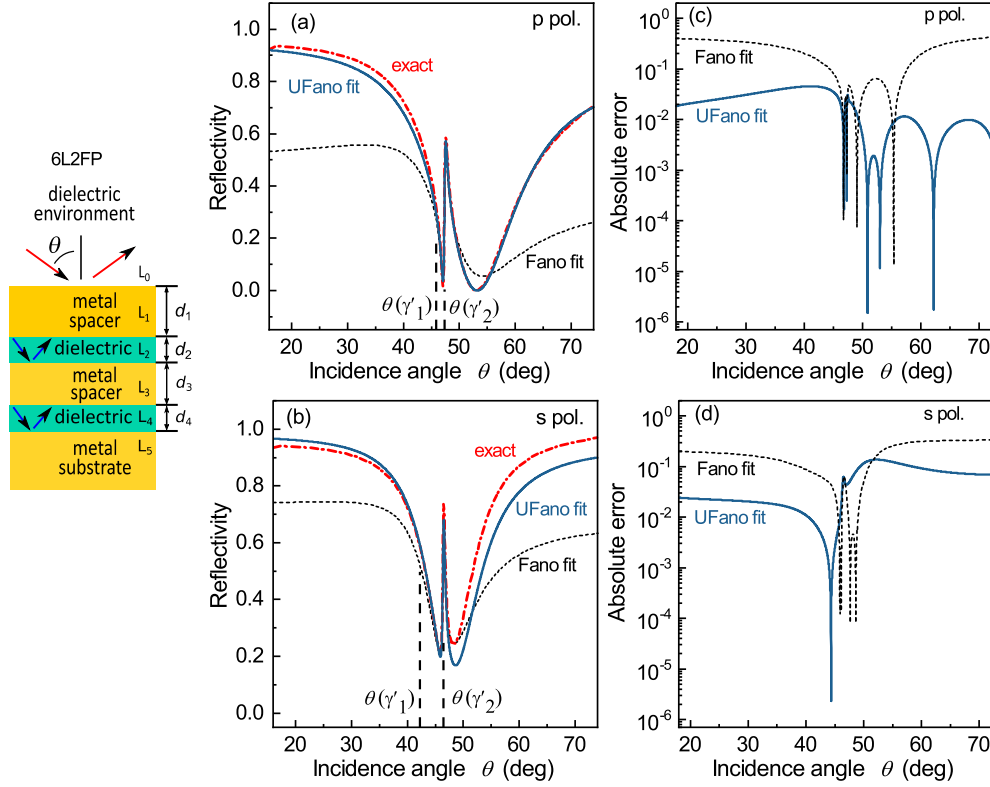


FIG. 8. Exact reflectivity spectra $|r_{0,s}|^2$ (red bold dots), and “UFano” (blue solid line) and “Fano” (black dashed line) approximations in the six-layer MIMIM structure, which support excitation of radiative Fabry-Pérot modes for (a) p and (b) s polarizations (6L2FP structure). The absolute error of the approximations for (c) p and (d) s polarizations.

$o_{21}(\alpha) = (\xi_l + \zeta_l)v_{l+1}[1 - (1 - \bar{\sigma}_l)v_l^{-2}r_{l,l-1}^{-1}]$ in the “UFano” case. The approximations are compared with exact calculations in Fig. 8. The Fabry-Pérot modes are excited for both polarizations. As can be clearly seen in the figure, the interference between the broad MIM1 and narrow MIM2 Fabry-Pérot modes results in the appearance of Fano line shapes in the reflectivity spectra. As the polarization state affects the mutual position of the resonances, the asymmetry of the resonance features differs for p and s polarizations. In the p polarization case, the positions of the MIM1 and MIM2 Fabry-Pérot modes are detuned that leads to the asymmetric Fano line. In the s polarization case, inside a broad reflection dip a narrow reflectivity peak appears near $\alpha = \gamma'_2$; this line shape corresponds to the symmetric electromagnetically induced transparency (EIT) or plasmon-induced transparency (PIT) [55].

As can be seen in Fig. 8, the “UFano” approximation reproduces very well the exact data in a wide angular region. The error in the “Fano” approximation falls in the same level as that of the “UFano” approximation in the narrower region of $\gamma'_2 \pm 0.02$ RIU.

In the “UFano” approach, the Fano behavior of the outcoupling coefficient ρ_2 and ρ_4 results in the partial transformation of resonance components into nonresonance ones and nonresonance components into resonance ones. Analyzing the difference in the “Fano” and “UFano” approaches, we conclude that the outcoupling mechanism for the field in interference resonators plays an important role in formation of the nonresonance background in the total response.

The absolute errors of the approximations are demonstrated in Figs. 8(c) and 8(d) as functions of θ . The “UFano” absolute error does not exceed 0.046 and 0.023 in the broad angular region of 18.0° – 72.0° and 18.0° – 46.2° for p and s polarizations, respectively. The “Fano” approximation shows the same error values in much narrower regions of 46.0° – 50.7° and 46.3° – 45.2° , respectively.

V. CONCLUSIONS

In the present work, approximate expressions of the field amplitudes around the resonances in multilayer interference resonance structures were obtained by using the 2×2 transfer matrix approach. Based on the expressions the spatial CM models were developed for three-, four-, and six-layer structures that support a variety of single and coupled interference modes.

Our CM formalism confirms that the fields excited in the resonators are characterized by both the resonance and nonresonance components; this feature becomes particularly important in lossy or low- Q structures. From the analysis of the resonance effects associated with the excitation of interference modes, it was found that coupling of the external fields with the fields of interference modes is affected by the interference, and the coupling coefficients are expressed in terms of the Fano functions. The resonance behavior of incoupling and outcoupling of total fields from interference resonators modifies dramatically the ratio of the outcoupled resonant and nonresonant fields in the out-of-resonance con-

ditions. This is in severe contrast to the conventional CMT, in which the coupling coefficients are assumed to be constants, resulting in large discrepancies with exact solutions in low- Q interference systems. Our finding is extremely important to implement appropriately the spatial CMT to the interference resonators.

To examine the validity of the approximate expressions and corresponding CM models in simulation of low- Q and high- Q interference structures, the approximate expressions of the rigorous solutions of the EM theory are represented in two forms, i.e., general Fano formulas with constant coefficients (“Fano” case) and composite Fano formulas, in which the outcoupling coefficients themselves take the form of the Fano functions (“UFano” case). Numerical results obtained by both the “Fano” and “UFano” approaches are compared with rigorous numerical calculations for planar multilayer structures that support excitation of WG and Fabry-Pérot modes, as well as the coupling of two Fabry-Pérot modes in a MIMIM structure. To produce both the symmetric and asymmetric line shapes, various loss levels were introduced to the structures by appropriately choosing the optical constants. The results of error analysis revealed that the “UFano” approximation brings about the line shapes in excellent agreement with those obtained by the rigorous calculations. The “Fano” approximation with the constant coefficients exhibits a good accuracy in substantially narrower regions in the resonance vicinity as compared to those of the “UFano” approximation. The applicability of the “Fano” approach and, to some extent, of the conventional CMT was found to be limited by the following main factors that affect the approximation quality in the resonance vicinity: the mode density, which increases with increasing the thickness of the interference layer, and the resonance width, which is mainly determined by the absorption in layers. To achieve the best approximation results, the detuning of neighboring modes should be much larger than the resonance width. Alternatively, the neighboring modes should be also appropriately described in the CM model. Although the applicability of this approach is demonstrated in the single- and double-mode cases, the CM models can be further extended to structures supporting an arbitrary number of modes for both the spatial and time domain.

Several intrinsic features of the multilayer interference resonators were revealed from our CM analysis. The resonance behavior of far-field enhancement spectra in the interference resonators does not reflect directly the behavior of local total FE inside the resonators. Our theoretical findings can be confirmed experimentally using, e.g., fluorescence spectroscopy [34,56,57]. Inspired by the physical interpretation within the spatial CM models developed in the present work, the condition of critical coupling was correctly formulated and the phenomenon of the resonance shift due to the mode self-coupling was explained. The Fano coefficients explicitly given by the geometrical and optical parameters of the multilayer interference structures allow one to derive analytical expressions for main resonance properties, i.e., the position and width of resonance, maximum FE, resonance slope, sensitivity to the changes in optical characteristics of environment, etc. The analytical expressions for the pole and zero parameters suggest that the self-coupling of the resonator fields due to multiple reflections in the adjacent layers is the main factor,

which leads to the resonance shifts from the intrinsic positions and to the changes in the resonance line shapes.

Indeed, the far-field spectra can still be fitted by general Fano formulas and, therefore, approximated by the conventional phenomenological CO and CM models dealing with resonance components only and constant coupling coefficients. However, in contrast to the spatial CMT developed in this work, conventional CO and CM models are not able to catch underlying physical effects. Therefore, our rigorous CM formulations are helpful to gain physical insights into the effects of coupling between the local electric fields inside the interference resonators and can be used to further develop a general CM formulation for complex coupled resonance systems.

ACKNOWLEDGMENTS

This work is supported by the Ministry of Science and Higher Education of Russian Federation (State assignment to FSRC “Crystallography and Photonics” RAS) and by the Russian Foundation for Basic Research (Project No. 18-29-20006). This work is also partially supported by JSPS KAKENHI Grant No. 19K05307.

APPENDIX A: ELECTROMAGNETIC THEORY FOR LAYERED MEDIA

In this appendix we provide a detailed formulation of the 2×2 transfer matrix approach used for derivation of analytical expressions approximating the field amplitudes.

1. Single interface

The light propagation in real structures is influenced by surface and material inhomogeneities, which can cause absorption, scattering, and attenuation [58]. In the present derivations, we assume that multilayer structures are composed of ideal thin films, without the inhomogeneities, and implement approaches of the rigorous EM theory of wave propagation in layered media [8].

Let us consider a general case of a p - or s -polarized plane wave incident on an interface $I_{l,l+1}$ between two semi-infinite homogeneous layers L_l and L_{l+1} through the layer L_l as shown in Fig. 9.

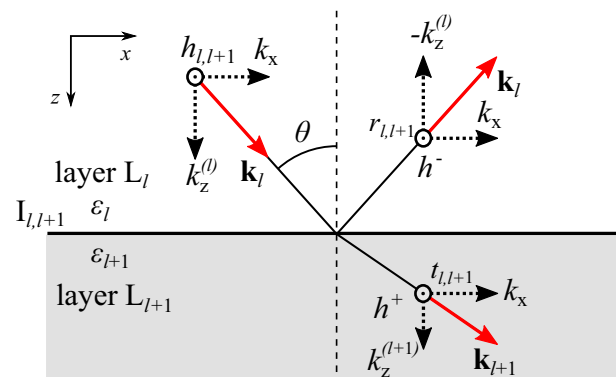


FIG. 9. Refraction and reflection of plane waves at the interface between two media.

Suppose that the x and y axes are parallel and perpendicular, respectively, to the plane of incidence. In such a coordinate system, the harmonic field in the structure can be written as $\mathbf{H}_l = (0, h_l, 0) \exp(-i\omega t)$, where the subscript l denotes the layer number, ω is the angular frequency. The layer L_l is characterized by the refractive index n_l and the dielectric constant $\varepsilon_l = n_l^2$. Assume that EM waves propagate in the x - z plane, so the total field is uniform along the y axis. In the case of a source-free media, the steady-state wave equation for the field h_l is represented by the scalar Helmholtz equation

$$\frac{\partial^2 h_l}{\partial x^2} + \frac{\partial^2 h_l}{\partial z^2} + k_0^2 \varepsilon_l(z) h_l = 0. \quad (\text{A1})$$

The equation for a plane wave $h_{l,l+1}(x, z)$ in L_l translating the field excitations on $I_{l,l+1}$ can be written as

$$h_{l,l+1}(x, z) = H_{l,l+1} \exp[ik_0(\alpha x + \beta_l z)]. \quad (\text{A2})$$

For a propagating wave, which is incident at an angle θ to the normal of $I_{l,l+1}$ in L_l , the x and z components of the propagation constant are given as $k_x = k_0 \alpha = k_0 \sqrt{\varepsilon_l} \sin \theta$ and $k_z = k_0 \beta_l = k_0 \sqrt{\varepsilon_l} \cos \theta$, respectively.

The plane wave $h_{l,l+1}$ generates two outcoupling plane waves in both layers. For a given α , the total field h_l in the considered structure is found as a solution of Eq. (A1):

$$h_l(x, z) = \begin{cases} h_{l,l+1}(x, z) + h^-(x, z), & z \in L_l, \\ h^+(x, z), & z \in L_{l+1}. \end{cases} \quad (\text{A3})$$

The fields of the reflected h^- and transmitted h^+ waves are expressed as $h^-(x, z) = r_{l,l+1}(\alpha) H_{l,l+1} \exp[ik_0(\alpha x - \beta_l z)]$ and $h^+(x, z) = t_{l,l+1}(\alpha) H_{l,l+1} \exp[ik_0(\alpha x + \beta_{l+1} z)]$ with complex reflection $r_{l,l+1}$ and transmission $t_{l,l+1}$ coefficients, respectively. The polarization-dependent reflection coefficients $r_{l,l+1}$ can be easily determined by the transfer matrix approach [7] in the case of p and s polarizations, respectively, as

$$r_{l,l+1}^p = \frac{\beta_l/\varepsilon_l - \beta_{l+1}/\varepsilon_{l+1}}{\beta_l/\varepsilon_l + \beta_{l+1}/\varepsilon_{l+1}} \quad \text{and} \quad r_{l,l+1}^s = \frac{\beta_l - \beta_{l+1}}{\beta_l + \beta_{l+1}}. \quad (\text{A4})$$

The relations $r_{l+1,l} = -r_{l,l+1}$, $t_{l,l+1} = 1 + r_{l,l+1}$ and $t_{l+1,l} = 1 + r_{l+1,l}$ are fulfilled regardless of the polarization state of the incident wave.

2. Three-layer system

According to Fig. 1, the total field h_l in L_l can be represented as the interference of backward h_l^- and forward h_l^+ waves, $h_l = h_l^- + h_l^+$, where

$$\begin{aligned} h_l^- &= (r_{l,l+1} H_{l,l+1} + t_{l+1,l} H_{l+1,l}) \exp\{ik_0[\alpha x - \beta_l(z - d_l)]\}, \\ h_l^+ &= (t_{l-1,l} H_{l-1,l} + r_{l,l-1} H_{l,l-1}) \exp\{ik_0(\alpha x + \beta_l z)\}. \end{aligned} \quad (\text{A5})$$

The complex amplitudes H_l^- and H_l^+ of the h_l^- and h_l^+ waves, respectively, are derived by the following

expressions:

$$\begin{aligned} H_l^- &= r_{l,l+1} H_{l,l+1} + t_{l+1,l} H_{l+1,l} = H_{l,l-1}/v_l, \\ H_l^+ &= t_{l-1,l} H_{l-1,l} + r_{l,l-1} H_{l,l-1} = H_{l,l+1}/v_l. \end{aligned} \quad (\text{A6})$$

Based on the relations (A6), the following relations between the complex field amplitudes of the waves at $I_{l-1,l}$ and $I_{l,l+1}$ can be written in a vector form, respectively:

$$H_{l,l-1} = v_l [t_{l+1,l} \quad r_{l,l+1}] \begin{bmatrix} H_{l+1,l} \\ H_{l,l+1} \end{bmatrix}, \quad (\text{A7})$$

$$H_{l,l+1} = v_l [t_{l-1,l} \quad r_{l,l-1}] \begin{bmatrix} H_{l-1,l} \\ H_{l,l-1} \end{bmatrix}. \quad (\text{A8})$$

The change in the amplitude of a wave in L_l for a round-trip distance $2d_l$ is characterized by the squared transfer coefficient v_l^2 . The relations between the complex amplitudes of the forward and backward incident plane waves at $I_{l-1,l}$ and $I_{l,l+1}$ can be written in the 2×2 transfer matrix form as

$$\begin{bmatrix} H_{l,l-1} \\ H_{l-1,l} \end{bmatrix} = \begin{bmatrix} A_l & B_l \\ C_l & D_l \end{bmatrix} \begin{bmatrix} H_{l+1,l} \\ H_{l,l+1} \end{bmatrix}, \quad (\text{A9})$$

where the coefficients of the transfer matrix are given by

$$\begin{aligned} A_l &= v_l t_{l+1,l}, & C_l &= -\frac{v_l r_{l,l-1} t_{l+1,l}}{t_{l-1,l}}, \\ B_l &= v_l r_{l,l+1}, & D_l &= \frac{1 - v_l^2 r_{l,l-1} r_{l,l+1}}{v_l t_{l-1,l}}. \end{aligned} \quad (\text{A10})$$

The coefficients A_l , B_l , C_l , D_l in Eq. (A10) take the same forms for both polarizations. The expressions for s and p polarizations can be obtained only by using r and t coefficients appropriate for the polarization state. Therefore, the polarization-dependent boundary conditions for the total field and its normal derivatives at the interfaces depending on the polarization state of the incident wave are automatically satisfied.

When the wave $h_{l+1,l}$ is absent ($H_{l+1,l} = 0$), the field at the interface $I_{l,l+1}$ is given by

$$H_{l,l+1} = D_l^{-1} H_{l-1,l} = \chi_l v_l t_{l-1,l} H_{l-1,l}, \quad (\text{A11})$$

and the amplitude of the backward wave at $I_{l-1,l}$ is given by

$$H_{l,l-1} = B_l H_{l,l+1} = \chi_l v_l^2 t_{l-1,l} r_{l,l+1} H_{l-1,l}, \quad (\text{A12})$$

where $\chi_l(\alpha) = (1 - v_l^2 r_{l,l-1} r_{l,l+1})^{-1}$ is the complex coefficient describing the field generation in the layer L_l by the exciting wave of amplitude $H_{l-1,l}$ as a result of multiple reflections inside the layer L_l between $I_{l-1,l}$ and $I_{l,l+1}$.

The total field h_l in the middle layer L_l is represented as the interference of two plane waves with the complex amplitudes $H_{l,l+1} = \chi_l v_l t_{l-1,l} H_{l-1,l}$ and $H_{l,l-1} = \chi_l v_l^2 t_{l-1,l} r_{l,l+1} H_{l-1,l}$ that propagate in opposite directions

along the z axis and can be written as

$$h_l(x, z, \alpha) = H_{l,l+1}(\alpha) \exp(ik_0\alpha x) \{r_{l,l+1} \exp[-ik_0\beta_l(z - d_l)] + \exp[ik_0\beta_l(z - d_l)]\}. \quad (\text{A13})$$

The total transmission and reflection coefficients for the three-layer structure are found as $t_{l-1,l+1} = h_{l+1}^+/h_{l-1}^+$ and $r_{l-1,l+1} = h_{l-1}^-/h_{l-1}^+$, respectively, and can be estimated using Eq. (A6).

The enhancement of interference field amplitude, $H_{l,l+1}/H_{l-1,l}$, according to Eq. (A11), is proportional to $\chi_l(\alpha) = \sigma_l^{-1}$. From the definition, it follows $0 \leq |\sigma_l| \leq 2$. The dispersion relation (4) can be written in the following form by introducing polarization-dependent and polarization-independent coefficients:

$$k_0\beta_l(\gamma)d_l = \pi m + i \ln \frac{\beta_l(\gamma)\bar{w}_{l,l-1} - \beta_{l-1}(\gamma)\bar{w}_{l-1,l}}{(\varepsilon_l - \varepsilon_{l-1})^{1/2}} \bar{p}_{l,l-1} + i \ln \frac{\beta_l(\gamma)\bar{w}_{l,l+1} - \beta_{l+1}(\gamma)\bar{w}_{l+1,l}}{(\varepsilon_l - \varepsilon_{l+1})^{1/2}} \bar{p}_{l,l+1}, \quad m \in \mathbb{Z} \quad (\text{A14})$$

where polarization-dependent coefficient $\bar{w}_{l,k}$ is obtained from the relation (3) as $\bar{w}_{l,k} = 1$ in the case of s polarization and $\bar{w}_{l,k} = (\varepsilon_k/\varepsilon_l)^{1/2}$ in the case of p polarization.

Depending on the effective refractive index γ of a resonant mode supported by the structure, where γ satisfies Eq. (4), the dispersion relation (4) can be represented in the well-known forms. For example, in the case $\text{Re}(\varepsilon_{l-1}), \text{Re}(\varepsilon_{l+1}) < \gamma'^2 < \text{Re}(\varepsilon_l)$, Eq. (A14) reduces to the planar WG mode excitation

oscillations in four-layer structures can be expressed in the matrix form as

$$\begin{bmatrix} H_{l-1,l-2} \\ H_{l-2,l-1} \end{bmatrix} = \begin{bmatrix} A_{l-1}A_l - B_{l-1}C_l & A_{l-1}B_l + B_{l-1}D_l \\ C_{l-1}A_l + D_{l-1}C_l & C_{l-1}B_l + D_{l-1}D_l \end{bmatrix} \begin{bmatrix} H_{l+1,l} \\ H_{l,l+1} \end{bmatrix}. \quad (\text{A18})$$

In the case of absence of the wave $h_{l+1,l}$ ($H_{l+1,l} = 0$) incoming in the outer most layer, the complex amplitude $H_{l,l+1}$ of the interference field is expressed as the Fano resonance

$$H_{l,l+1} = (C_{l-1}B_l + D_{l-1}D_l)^{-1} H_{l-2,l-1}, \quad (\text{A18})$$

and the complex amplitude $H_{l-1,l-2}$ of the field outcoupled from the structure is given by

$$H_{l-1,l-2} = (A_{l-1}B_l + B_{l-1}D_l) H_{l,l+1}. \quad (\text{A19})$$

The total transmission and reflection coefficients for the four-layer structure are found as $t_{l-2,l+1} = h_{l+1}^+/h_{l-2}^+$ and $r_{l-2,l+1} = h_{l-2}^-/h_{l-2}^+$. The coefficients can be expressed using Eq. (A6) as $t_{l-2,l+1} = t_{l,l+1} H_{l,l+1}/H_{l-2,l-1}$ and $r_{l-2,l+1} = (r_{l-2,l-1} H_{l-2,l-1} + t_{l-1,l-2} H_{l-1,l-2})/H_{l-2,l-1}$, respectively.

APPENDIX B: SUMMARY OF CALCULATION PARAMETERS

1. Parameters of Fano approximations and resonance characteristics

The parameters of the Fano function in Eqs. (36) and (42) calculated using analytical expressions and some resonance characteristics of the reflectivity spectra are listed in Table II.

2. Parameters of the CM models

The coefficients of CM models obtained using analytical expressions are listed in Table III.

condition [44,48,49]

$$k_0\beta_l(\gamma)d_l = \pi m + \phi_{l,l-1} + \phi_{l,l+1}, \quad (\text{A15})$$

where the phase shifts of the waves by reflection from interfaces are found as $\phi_{l,k} = -\arccos \beta_l(\gamma)\bar{w}_{l,k}\bar{p}_{l,k}(\varepsilon_l - \varepsilon_k)^{-1/2}$.

The dispersion relation (4) can be also rewritten in an alternative form as two dispersion relations:

$$ik_0\beta_l(\gamma)d_l + i\pi m = \frac{1}{2} \ln \frac{1 + g_{l,l+1}}{1 - g_{l,l+1}} \frac{1 + g_{l,l-1}}{1 - g_{l,l-1}}, \quad (\text{A16})$$

$$ik_0\beta_l(\gamma)d_l + i\pi m = \frac{1}{2} \ln \frac{g_{l,l+1} + 1}{g_{l,l+1} - 1} \frac{g_{l,l-1} + 1}{g_{l,l-1} - 1},$$

where $g_{l,k} = \beta_k/(\bar{w}_{l,k}^2\beta_l)$, $m \in \mathbb{Z}$. Based on the definitions of the principal values of the inverse hyperbolic tangent and cotangent, the relations (A16) can then be reduced to the dispersion relations for symmetric and antisymmetric coupled modes generated by the coupling between the interface SPPs in metal-insulator-insulator (MIM) and insulator-metal-insulator structures [50], respectively:

$$\text{artanh}(g_{l,l+1}) + \text{artanh}(g_{l,l-1}) - ik_0\beta_l(\gamma)d_l = 0,$$

$$\text{arcoth}(g_{l,l+1}) + \text{arcoth}(g_{l,l-1}) - ik_0\beta_l(\gamma)d_l = 0. \quad (\text{A17})$$

3. Four-layer system

The approximation approach can be extended to combinations of multilayer structures, which support resonant modes. In the 2×2 transfer matrix formalism, any multilayer system can be reduced to a three-layer system with an effective middle layer. The relations for the transfer of amplitudes of field

TABLE II. Fano coefficients and some resonance characteristics of the samples.

	3LWG (<i>p</i> polar.)	3LWG (<i>s</i> polar.)	4LWG (<i>p</i> polar.)	4LWG (<i>s</i> polar.)
γ (RIU)	$1.1450140 + i4.6 \times 10^{-5}$	$1.2633274 + i8.3 \times 10^{-5}$	$1.1450140 + i4.6 \times 10^{-5}$	$1.263327352 + i8.3 \times 10^{-5}$
γ_{zero} (RIU)	$1.1449804 + i0.143548$	$1.2633123 + i0.143111$	$1.1451444 - i4.5 \times 10^{-4}$	$1.263324533 + i2.1 \times 10^{-5}$
γ_{pole} (RIU)	$1.1450140 + i4.6 \times 10^{-5}$	$1.2633274 + i8.3 \times 10^{-5}$	$1.1451406 + i5.3 \times 10^{-4}$	$1.263324531 + i1.4 \times 10^{-4}$
κ	$1.2 \times 10^{-5} - i0.062664$	$2 \times 10^{-6} - i0.056608$	$1.2 \times 10^{-5} - i0.062664$	$2 \times 10^{-6} - i0.056608$
$r_{1,2}$	$0.252924 + i0.967458$	$-0.046396 + i0.998694$	$0.252924 + i0.967458$	$-0.046396 + i0.998694$
$r_{0,1}$	—	—	$-0.252931 - i0.967484$	$0.046406 - i0.998923$
W	—	—	$-0.247783 - i0.954711$	$0.046288 - i0.997229$
P	—	—	$0.006830 - i0.001766$	$0.000848 + i3.9 \times 10^{-5}$
Mode FE	2.48569×10^7	5.68531×10^6	272.5	2350.7
FWHM	9.1×10^{-5} RIU	1.66×10^{-4} RIU	0.06356° (0.000717 RIU)	0.02035° (0.000191 RIU)
θ_{res}	—	—	49.76754° (1.145145 RIU)	57.37492° (1.263324 RIU)
R_{min}	—	—	0.68978	0.02342
q	$3.4 \times 10^{-5} - i0.143502$	$1.5 \times 10^{-5} - i0.143028$	$-3.8 \times 10^{-6} + i9.8 \times 10^{-4}$	$-2 \times 10^{-9} - i1.19 \times 10^{-4}$
\bar{q}	0.7	0.2	0.0	0.0
g	1.0×10^7	3.0×10^6	0.7	3.4
	4LMWG (<i>p</i> polar.)	4LMWG (<i>s</i> polar.)	4LFP (<i>p</i> polar.)	4LFP (<i>s</i> polar.)
γ (RIU)	$1.0101614 + i3.62 \times 10^{-4}$	$1.273461 + i4.03 \times 10^{-4}$	$0.735539 + i8.79 \times 10^{-4}$	$0.724375 + i6.56 \times 10^{-4}$
γ_{zero} (RIU)	$1.014226 - i1.532 \times 10^{-3}$	$1.277488 - i1.42 \times 10^{-4}$	$0.769432 + i1.183 \times 10^{-3}$	$0.747256 + i5.741 \times 10^{-3}$
γ_{pole} (RIU)	$1.012773 + i3.055 \times 10^{-3}$	$1.277115 + i1.789 \times 10^{-3}$	$0.745827 + i1.6714 \times 10^{-2}$	$0.737867 + i1.2697 \times 10^{-2}$
κ	$5.14 \times 10^{-4} - i0.031342$	$-9.2 \times 10^{-5} - i0.057665$	$-1.558 \times 10^{-4} - i0.065391$	$-1.551 \times 10^{-4} - i0.065401$
r_{12}	$-0.829073 - i0.539906$	$0.970776 + i0.221950$	$-0.873801 - i0.467291$	$0.924505 + i0.362686$
r_{01}	$0.829079 + i0.539909$	$-0.970827 - i0.221963$	$0.904473 + i0.407593$	$-0.976836 - i0.1958687$
W	$0.668086 + i0.518163$	$-0.930130 - i0.261813$	$0.475136 + i0.299395$	$-0.736995 - i0.237730$
P	$0.083656 - i0.083881$	$0.019056 - i0.049731$	$0.329490 - i0.213515$	$0.254572 - i0.284414$
Mode FE	9.2	9.2	2.5	0.7
FWHM	0.3923° (0.00756 RIU)	0.234037° (0.003211 RIU)	3.47844° (0.03892 RIU)	1.418° (0.016427 RIU)
θ_{res}	42.54844° (1.014320 RIU)	58.38612° (1.277400 RIU)	49.70989° (0.762780 RIU)	48.29671° (0.746600 RIU)
R_{min}	0.39327	0.04257	0.65898	0.38955
q	$-1.453 \times 10^{-3} + i4.587 \times 10^{-3}$	$-3.73 \times 10^{-4} + i1.931 \times 10^{-3}$	$-0.023605 + i0.015531$	$-9.389 \times 10^{-3} + i6.956 \times 10^{-3}$
\bar{q}	-0.5	-0.2	-1.4	-0.7
g	0.3	0.8	5.0×10^{-3}	0.2

TABLE III. CM coefficients.

	3LWG (<i>p</i> polar.)	3LWG (<i>s</i> polar.)		4LWG (<i>p</i> polar.)	4LWG (<i>s</i> polar.)
γ (RIU)	$1.1450140 + i4.6 \times 10^{-5}$	$1.2633274 + i8.3 \times 10^{-5}$	γ (RIU)	$1.1450140 + i4.6 \times 10^{-5}$	$1.263327352 + i8.3 \times 10^{-5}$
κ	$1.2 \times 10^{-5} - i0.062664$	$2 \times 10^{-6} - i0.056608$	κ	$1.2 \times 10^{-5} - i0.062664$	$2 \times 10^{-6} - i0.056608$
$r_{1,2}$	$0.252924 + i0.967458$	$-0.046396 + i0.998694$	$r_{0,1}$	$-0.252931 - i0.967484$	$0.046406 - i0.998923$
τ_2	$1.574152 + i0.115153$	$-0.953031 + i0.998573$	$\tau_{1,2}$	$-0.000208 + i0.116852$	$0.6 \times 10^{-5} + i0.041199$
ρ_2	$-1.198467 + i0.221379$	$1.045791 - i0.998116$	ρ_1	$-0.037519 + i0.088288$	$-0.021504 + i0.018700$
			η_1	$-0.006852 + i0.001778$	$-0.000849 - i3.9 \times 10^{-5}$
			$\rho_{2,1}$	$0.113413 - i0.029648$	$0.041162 + i0.001917$
	4LMWG (<i>p</i> polar.)	4LMWG (<i>s</i> polar.)		4LFP (<i>p</i> polar.)	4LFP (<i>s</i> polar.)
γ (RIU)	$1.0101614 + i3.62 \times 10^{-4}$	$1.273461 + i4.03 \times 10^{-4}$	γ (RIU)	$0.735539 + i8.79 \times 10^{-4}$	$0.724375 + i6.56 \times 10^{-4}$
κ	$5.14 \times 10^{-4} - i0.031342$	$-9.2 \times 10^{-5} - i0.057665$	κ	$-1.558 \times 10^{-4} - i0.065391$	$-1.551 \times 10^{-4} - i0.065401$
$r_{0,1}$	$0.829079 + i0.539909$	$-0.970827 - i0.221963$	$r_{0,1}$	$0.904473 + i0.407593$	$-0.976836 - i0.1958687$
$\tau_{1,2}$	$-0.244576 + i0.282601$	$0.089222 + i0.136103$	$\tau_{1,2}$	$0.290527 - i0.680546$	$0.097534 - i0.345819$
ρ_1	$-0.147177 + i0.115744$	$0.614141 + i0.229315$	ρ_1	$-0.178742 + i0.199905$	$1.130752 + i0.589948$
η_1	$-0.083317 + i0.091190$	$-0.017968 + i0.050660$	η_1	$-0.355990 + i0.301129$	$-0.232426 + i0.363769$
$\rho_{2,1}$	$-0.015621 + i0.360440$	$0.118846 - i0.086951$	$\rho_{2,1}$	$0.240462 - i0.458659$	$-0.145145 + i0.449637$

- [1] A. Kuznetsov, A. Miroschnichenko, M. Brongersma, Y. Kivshar, and B. Lukyanchuk, Optically resonant dielectric nanostructures, *Science* **354**, aag2472 (2016).
- [2] P. Törmä and W. L. Barnes, Strong coupling between surface plasmon polaritons and emitters: A review, *Rep. Prog. Phys.* **78**, 013901 (2015).
- [3] D. K. Gramotnev and S. I. Bozhevolnyi, Plasmonics beyond the diffraction limit, *Nat. Photonics* **4**, 83 (2010).
- [4] P. Lalanne, W. Yan, K. Vynck, C. Sauvan, and J.-P. Hugonin, Light interaction with photonic and plasmonic resonances, *Laser Photon. Rev.* **12**, 1700113 (2018).
- [5] B. Gallinet and O. J. F. Martin, Influence of electromagnetic interactions on the line shape of plasmonic Fano resonances, *ACS Nano* **5**, 8999 (2011).
- [6] N. J. Halas, S. Lal, S. Link, P. Nordlander, and W. S. Chang, Plasmons in strongly coupled metallic nanostructures, *Chem. Rev.* **111**, 3913 (2011).
- [7] P. Markos and C. M. Soukoulis, *Wave Propagation from Electrons to Photonic Crystals and Left-Handed Materials* (Princeton University Press, Princeton, 2008).
- [8] P. Yeh, A. Yariv, and C.-S. Hong, Electromagnetic propagation in periodic stratified media. I. General theory, *J. Opt. Soc. Am.* **67**, 423 (1977).
- [9] L. Li, Use of Fourier series in the analysis of discontinuous periodic structures, *J. Opt. Soc. Am. A* **13**, 1870 (1996).
- [10] A. Taflov and S. C. Hagness, *Computational Electrodynamics: The Finite-Difference Time-Domain Method* (Artech House, Boston, 2005).
- [11] J.-M. Jin, *The Finite Element Method in Electromagnetics* (Wiley, New York, 1993).
- [12] D. V. Nesterenko, Modeling of diffraction of electromagnetic waves on periodic inhomogeneities by a finite element method coupled with the Rayleigh expansion, *Optoelectronics Instrum. Data Proc.* **47**, 68 (2011).
- [13] U. Fano, Sullo spettro di assorbimento dei gas nobili presso il limite dello spettro darco, *Nuovo Cimento* **12**, 154 (1935).
- [14] U. Fano, Effects of configuration interaction on intensities and phase shifts, *Phys. Rev.* **124**, 1866 (1961).
- [15] D. V. Nesterenko, S. Hayashi, and Z. Sekkat, Asymmetric surface plasmon resonances revisited as Fano resonances, *Phys. Rev. B* **97**, 235437 (2018).
- [16] F. Wu, J. Wu, Z. Guo, H. Jiang, Y. Sun, Y. Li, J. Ren, and H. Chen, Giant Enhancement of the Goos-Hänchen Shift Assisted by Quasibound States in the Continuum, *Phys. Rev. Appl.* **12**, 014028 (2019).
- [17] F. Wu, M. Luo, J. Wu, C. Fan, X. Qi, Y. Jian, D. Liu, S. Xiao, G. Chen, H. Jiang *et al.*, Dual quasibound states in the continuum in compound grating waveguide structures for large positive and negative Goos-Hänchen shifts with perfect reflection, *Phys. Rev. A* **104**, 023518 (2021).
- [18] H. A. Haus, *Waves and Fields in Optoelectronics* (Prentice-Hall, Englewood Cliffs, NJ, 1984).
- [19] S. Fan, W. Suh, and J. D. Joannopoulos, Temporal coupled-mode theory for the Fano resonance in optical resonators, *J. Opt. Soc. Am. A* **20**, 569 (2003).
- [20] Z. Ruan and S. Fan, Temporal coupled-mode theory for Fano resonance in light scattering by a single obstacle, *J. Phys. Chem. C* **114**, 7324 (2010).
- [21] Q. Li, G. Moille, H. Taheri, A. Adibi, and K. Srinivasan, Improved coupled-mode theory for high-index-contrast photonic platforms, *Phys. Rev. A* **102**, 063506 (2020).
- [22] B. E. Little, S. T. Chu, H. A. Haus, J. Foresi, and J.-P. Laine, Microring resonator channel dropping filters, *J. Lightwave Technol.* **15**, 998 (1997).
- [23] M. Popovic, C. Manolatos, and M. Watts, Coupling-induced resonance frequency shifts in coupled dielectric multi-cavity filters, *Opt. Express* **14**, 1208 (2006).
- [24] M. L. Cooper and S. Mookherjee, Numerically-Assisted coupled-mode theory for silicon waveguide couplers and arrayed waveguides, *Opt. Express* **17**, 1583 (2009).
- [25] T. Zentgraf, S. Zhang, R. F. Oulton, and X. Zhang, Ultranarrow coupling-induced transparency bands in hybrid plasmonic systems, *Phys. Rev. B* **80**, 195415 (2009).
- [26] E. S. Hosseini, S. Yegnanarayanan, A. H. Atabaki, M. Soltani, and A. Adibi, Systematic design and fabrication of high- Q single-mode pulley-coupled planar silicon nitride microdisk resonators at visible wavelengths, *Opt. Express* **18**, 2127 (2010).
- [27] M. Soltani, S. Yegnanarayanan, Qing Li, and A. Adibi, Systematic engineering of waveguide-resonator coupling for silicon microring/microdisk/racetrack resonators: Theory and experiment, *IEEE J. Quantum Electron.* **46**, 1158 (2010).
- [28] Q. Li, M. Davanco, and K. Srinivasan, Efficient and low-noise single-photon-level frequency conversion interfaces using silicon nanophotonics, *Nat. Photon.* **10**, 406 (2016).
- [29] Z. Ruan, Spatial mode control of surface plasmon polariton excitation with gain medium: From spatial differentiator to integrator, *Opt. Lett.* **40**, 601 (2015).
- [30] Y. S. Joe, A. M. Satanin, and C. S. Kim, Classical analogy of Fano resonances, *Phys. Scr.* **74**, 259 (2006).
- [31] L. Novotny, Strong coupling, energy splitting, and level crossings: A classical perspective, *Am. J. Phys.* **78**, 1199 (2010).
- [32] B. Gallinet, Model of coupled oscillators for Fano resonances, in *Fano Resonances in Optics and Microwaves*, edited by E. Kamenetskii, A. Sadreev, and A. Miroschnichenko (Springer, New York, 2018), pp. 109–136.
- [33] S. Hayashi, D. V. Nesterenko, and Z. Sekkat, Waveguide-coupled surface plasmon resonance sensor structures: Fano lineshape engineering for ultrahigh-resolution sensing, *J. Phys. D* **48**, 325303 (2015).
- [34] K. Motokura, M. Fujii, D. V. Nesterenko, Z. Sekkat, and S. Hayashi, Coupling of Planar Waveguide Modes in All-Dielectric Multilayer Structures: Monitoring the Dependence of Local Electric Fields on the Coupling Strength, *Phys. Rev. Appl.* **16**, 064065 (2021).
- [35] Y. Lou, H. Pan, T. Zhu, and Z. Ruan, Spatial coupled-mode theory for surface plasmon polariton excitation at metallic gratings, *J. Opt. Soc. Am. B* **33**, 819 (2016).
- [36] T. F. Zhu, Y. H. Zhou, Y. J. Lou, H. Ye, M. Qiu, Z. C. Ruan, and S. H. Fan, Plasmonic computing of spatial differentiation, *Nat. Commun.* **8**, 15391 (2017).
- [37] Z. Ruan, H. Wu, M. Qiu, and S. Fan, Spatial control of surface plasmon polariton excitation at planar metal surface, *Opt. Lett.* **39**, 3587 (2014).
- [38] H. Feshbach, Unified theory of nuclear reactions, *Ann. Phys.* **5**, 357 (1958).

- [39] J. K. S. Poon and A. Yariv, Active coupled-resonator optical waveguides. I. Gain enhancement and noise, *J. Opt. Soc. Am. B* **24**, 2378 (2007).
- [40] H. Zhang and O. D. Miller, Quasinormal coupled mode theory, [arXiv:2010.08650](https://arxiv.org/abs/2010.08650).
- [41] C. Tao, J. Zhu, Y. Zhong, and H. Liu, Coupling theory of quasinormal modes for lossy and dispersive plasmonic nano-resonators, *Phys. Rev. B* **102**, 045430 (2020).
- [42] D. V. Nesterenko, S. Hayashi, and Z. Sekkat, Coupled-mode theory of field transfer processes in surface plasmon resonance structures, *J. Phys. Conf. Ser.* **1092**, 012097 (2018).
- [43] D. V. Nesterenko, Resonance characteristics of transmissive optical filters based on metal/dielectric/metal structures, *Comput. Opt.* **44**, 219 (2020).
- [44] D. Marcuse, *Theory of Dielectric Optical Waveguides* (Academic Press, New York, 1974).
- [45] C. Fabry and A. Pérot, Théorie et applications d'une nouvelle méthode de spectroscopie interférentielle, *Ann. Chim. Phys.* **16**, 115 (1899).
- [46] E. N. Economou, Surface plasmons in thin films, *Phys. Rev.* **182**, 539 (1969).
- [47] S. Hayashi and T. Okamoto, Plasmonics: Visit the past to know the future, *J. Phys. D* **45**, 433001 (2012).
- [48] P. K. Tien and R. Ulrich, Theory of prism-film coupler and thin-film light guides, *J. Opt. Soc. Am.* **60**, 1325 (1970).
- [49] A. Otto and W. Sohler, Modification of the total reflection modes in a dielectric film by one metal boundary, *Opt. Comm.* **3**, 254 (1971).
- [50] J. A. Dionne, L. A. Sweatlock, H. A. Atwater, and A. Polman, Plasmon slot waveguides: Towards chip-scale propagation with subwavelength-scale localization, *Phys. Rev. B* **73**, 035407 (2006).
- [51] R. D. Kekatpure, A. C. Hryciw, E. S. Barnard, and M. L. Brongersma, Solving dielectric and plasmonic waveguide dispersion relations on a pocket calculator, *Opt. Express* **17**, 24112 (2010).
- [52] D. V. Nesterenko, R. Pavelkin, S. Hayashi, Z. Sekkat, and V. Soifer, Fano approximation as a fast and effective way for estimating resonance characteristics of surface plasmon structures, *Plasmonics* **16**, 1001 (2021).
- [53] D. V. Nesterenko, R. A. Pavelkin, and S. Hayashi, Estimation of resonance characteristics of single-layer surface-plasmon sensors in liquid solutions using Fano's approximation in the visible and infrared regions, *Comput. Opt.* **43**, 596 (2019).
- [54] D. V. Nesterenko, Fano approximation for coupled modes in metal-dielectric multilayer structures, *J. Phys.: Conf. Ser.* **1368**, 052046 (2019).
- [55] K. Matsunaga, Y. Hirai, Y. Neo, T. Matsumoto, and M. Tomita, Tailored plasmon-induced transparency in attenuated total reflection response in a metal-insulator-metal structure, *Sci. Rep.* **7**, 17824 (2017).
- [56] B. Kang, K. Motokura, M. Fujii, D. V. Nesterenko, Z. Sekkat, and S. Hayashi, Fano resonant behaviour of waveguide mode in all-dielectric multilayer structure directly monitored by fluorescence of embedded dye molecules, *J. Opt.* **21**, 105006 (2019).
- [57] B. Kang, K. Motokura, M. Fujii, D. V. Nesterenko, Z. Sekkat, and S. Hayashi, Observation of Fano line shape in directional fluorescence emission mediated by coupled planar waveguide modes and interpretation based on Lorentz reciprocity, *AIP Adv.* **10**, 075302 (2020).
- [58] P. Nagpal, D. J. Norris, N. C. Lindquist, and S. H. Oh, Ultrasmooth patterned metals for plasmonics and metamaterials, *Science* **325**, 594 (2009).
- [59] K. M. McPeak, S. V. Jayanti, S. J. P. Kress, S. Meyer, S. Iotti, A. Rossinelli, and D. J. Norris, Plasmonic films can easily be better: Rules and recipes, *ACS Photonics* **2**, 326 (2015).